This is a preprint, the final version is subject to change, of the American Mineralogist (MSA)
Cite as Authors (Year) Title. American Mineralogist, in press.
DOI: https://doi.org/10.2138/am-2018-6256

Revision 2

Origin of the Fluorine- and Beryllium-Rich Rhyolites of the Spor Mountain Formation, Western Utah

Shane R. Dailey[1*] (shane.dailey@ttu.edu); Eric H Christiansen[1] (eric_christiansen@byu.edu); Michael J. Dorais[1] (dorais@byu.edu); Bart J. Kowallis[1] (bkowallis@byu.edu); Diego P. Fernandez[2] (diego.fernandez@utah.edu); Douglas M. Johnson[1] (doug.m.johnson@gmail.com)

[1] Department of Geological Sciences, Brigham Young University, Provo, UT 84602, U.S.A.

[2] Department of Geology and Geophysics, University of Utah, Salt Lake City, Utah 84112, U.S.A.

[*]Present address: Department of Geosciences, Texas Tech University, Lubbock, Texas 79409, U.S.A.

For Submission to American Mineralogist

April 2018

This is a preprint, the final version is subject to change, of the American Mineralogist (MSA)
Cite as Authors (Year) Title. American Mineralogist, in press.
DOI: https://doi.org/10.2138/am-2018-6256

Abstract

The Miocene rhyolites of the Spor Mountain Formation host Earth's largest beryllium deposit, which produced 85% of the world's beryllium in 2010. The fresh lava is extremely enriched in Be (up to 75 ppm in matrix glass). We have examined the rhyolite to better understand the Be enrichment. The Spor Mountain rhyolite contains ~40% quartz, ~40% sanidine, ~10% biotite, and ~10% plagioclase, along with accessory fluorite, columbite, euxenite, fergusonite, monazite, thorite, and zircon. Two types of rhyolite are present within the Spor Mountain Formation, a less evolved magma (1150 ppm Rb, 42 ppm Be, 0.7 wt% F in glass) and a more evolved magma (1710 ppm Rb, 75 ppm Be, 1.6 wt% F in glass).

Eruption temperatures estimated using two-feldspar (Elkins and Grove, 1990; Putirka, 2008; Benisek et al., 2010), plagioclase-liquid and alkali feldspar-liquid (Putirka, 2008), Ti-in-quartz (Thomas et al., 2010; Huang and Audétat, 2012; Thomas et al., 2015), biotite (Righter and Carmichael, 1996), and zircon saturation (Boehnke et al., 2013) geothermometers converge on 718 °C for the less evolved magma and 682 °C for the more evolved magma. Using the Ti-in-Qz equation of Huang and Audétat (2012), the pre-eruptive pressure of the Spor Mountain rhyolite system is estimated to be about 2 kbar at 700°C. Water content of the rhyolite melt was less than <5 wt%, based on the co-crystallization of all four major mineral phases at 700°C, and the magma was water undersaturated (Webster et al., 1987). Viscosity of the rhyolite was about $10^{6.2}$ Pa·s for the less evolved rhyolite and $10^{5.8}$ Pa·s for the more evolved rhyolite. Fluorine lowered the melt viscosity, though not by a large amount (less than 0.5 log units at 1.6 wt% F).

Partition coefficients for Be and other trace elements were determined for biotite, sanidine, plagioclase, and quartz from laser-ablation inductively coupled plasma mass spectrometry analyses. Partition coefficients for trace elements in feldspars from the Spor

Mountain rhyolite are generally higher than for feldspars from other silicic magmas, and lower for biotite. The enrichment of beryllium in the Spor Mountain rhyolite was aided by its high incompatibility in the major mineral phases, with a bulk partition coefficient <0.1.

Trace element models using the measured partition coefficients are inconsistent with accumulation of increments of melt formed by different degrees of partial melting, and cannot explain the great depletion of compatible elements. Rather, the trace element abundances and Nd and Sr isotopic compositions are consistent with derivation of rhyolite by ~25% partial melting of crust hybridized with mantle-derived components, followed by extensive fractional crystallization (75%). The combination of these magmatic processes set the stage for the formation of a world class beryllium deposit.

Keywords: Spor Mountain, partition coefficients, beryllium, fractional crystallization, topaz rhyolite, fluorine

Introduction

Beryllium is one of the lightest metals with a unique combination of properties, making it an ideal resource for a wide variety of applications, including military aircraft, aerospace, medical, and commercial markets. For example, on a weight-to-weight basis, beryllium is six times stronger than steel and can maintain its shape at extreme temperatures, even though it is only two-thirds as dense as aluminum. Beryllium also has a high specific heat (the highest of all metals), meaning it can absorb more heat than any other metal. Its relatively high X-ray transparency makes it an ideal candidate for medical and analytical applications. For these reasons, Be is on the "Strategic and Critical Materials" list of the U.S. Department of Defense and of the European Union (Thomason et al., 2013).

The Miocene rhyolite of the Spor Mountain Formation in western Utah (Lindsey, 1977; 1982; Christiansen et al., 1984) hosts one of the largest beryllium deposits in the world and was responsible for producing 85% of the beryllium mined worldwide in 2010 (Boland, 2012). Materion Brush Beryllium & Composites owns and operates the mine. The beryllium ore at Spor Mountain (in the form of bertrandite [$Be_4Si_2O_7(OH)_2$]) formed in a precursor tuff overlain by rhyolitic lava. The tuff is open-pit mined after the lava is removed.

The purpose of this study is to better understand the beryllium enrichment processes in the Spor Mountain rhyolite by (1) determining partition coefficients of beryllium and other important rare elements (e.g., Li, Sn, Mo, Nb, Ta) using element concentrations obtained by laser ablation inductively coupled plasma mass spectrometry (LA-ICP-MS); (2) constraining the pre-eruptive temperature, pressure, water content, and viscosity using electron microprobe (EMP) analysis of phenocrysts and glass, and LA-ICP-MS analysis of Ti in quartz; and (3) acquiring Nd and Sr isotopic compositions to understand the source of the distinctive F-rich magma. These

data are used to construct a model of magmatic origin and evolution to explain the extreme enrichment of Be (to as much as 75 ppm) and other incompatible elements in the rhyolite. We conclude that partial melting of a distinctive crustal source followed by extensive fractional crystallization set the stage for later low temperature hydrothermal processes, which further enriched the Be in the underlying tuff (up to 3000 ppm; Bikun, 1980; Foley et al., 2012) as discussed below.

Geologic Setting

Spor Mountain is a faulted and tilted block of Paleozoic sedimentary rocks fringed by Miocene volcanic rocks (Fig. 1). It lies about 120 km west of the topographic margin of the Great Basin—the northern part of the Basin and Range extensional province. Subduction-related Eocene-Oligocene volcanism was followed by two episodes of extension-related Miocene volcanism, including the rhyolites of the Spor Mountain Formation and the younger Topaz Mountain Rhyolite (Fig. 1). The Spor Mountain Formation consists of rhyolite plugs, lava flows and cogenetic tuff, which erupted ~21.7 m.y. ago onto Paleozoic sedimentary rock, chiefly limestone and dolomite, and the older, mid-Cenozoic volcanic rocks (Lindsey, 1979; Adams et al., 2009). The beryl and topaz-bearing Sheeprock Granite crops out 65 km east of Spor Mountain (Fig. 1) and is very similar to the Spor Mountain rhyolite in age (21 Ma) and in elemental, mineralogic, and isotopic composition (Christiansen et al., 1988); it is interpreted to be the intrusive equivalent of the topaz rhyolites of western Utah and we draw on comparisons with it throughout this paper.

Before about 45 Ma, shallow subduction of oceanic lithosphere under the western United States caused regional magmatism to cease and the Sevier and Laramide orogenies to form (e.g. Yonkee and Weil, 2015). Afterwards, between 45 and 22 Ma, the shallowly subducting oceanic

104 slab began to steepen and roll back (Severinghaus and Atwater, 1990; Best and Christiansen,
105 1991; Humphreys, 1995). As the descending oceanic slab dropped lower into the hotter
106 asthenosphere, it dehydrated over a large area initiating melting in the overlying mantle and
107 triggering the mid-Cenozoic ignimbrite flareup with its distinct subduction signatures in magmas
108 erupted far from the trench. (Best et al., 2016). As the oceanic slab continued to descend, the
109 Great Basin portion of the Basin and Range province experienced a transition from compression
110 to extension, which was accompanied by normal faulting and the characteristic bimodal
111 volcanism.

112 At 21.7 Ma (Adams et al., 2009), the Spor Mountain Formation is the oldest
113 representation of the extensional regime that currently dominates the Great Basin (Christiansen
114 et al., 1984). The eruption began as a series of ignimbrites and pyroclastic surges (the beryllium
115 tuff member) and ended with the extrusion of a thick lava flow (the porphyritic rhyolite member)
116 covering the tuff (Bikun, 1980). The tuff is 20 to 60 m thick, highly altered, and contains lithic
117 clasts of carbonate sedimentary rock that are silicified and partially altered to fluorite and calcite
118 (Lindsey, 1977), as well as mafic enclaves from a magma mixing event that is thought to have
119 triggered eruption (Christiansen and Venchiarutti, 1990). Bedding structures in the tuff show that
120 phreatomagmatic explosions were also important (Burt and Sheridan, 1981). The overlying lava
121 is as much as 500 m thick, but is everywhere truncated by erosion, so it may have been thicker.
122 The sharp basal contact with the tuff is marked by a flow breccia that contains lenses and blocks
123 of fresh vitrophyre. Most of the lava above the breccia is massive, flow layered, and
124 granophyrically devitrified with few cavities. Originally, the lava must have covered an area in
125 excess of about 40 km^2, based on the distribution today. Since its eruption, the Spor Mountain
126 rhyolite has been cut by Basin and Range normal faults, causing the tuff, lava flows, and

127 underlying Paleozoic strata to dip westward (Fig. 1). The faulting has made it difficult to
128 estimate the number of vents involved, although Lindsey (1979) and (1982) identified at least
129 three major vents.

130 The Spor Mountain rhyolite is a topaz rhyolite; these A-type rhyolites are typically
131 enriched in fluorine (>0.2 wt%) and incompatible elements and crystallize at low temperatures
132 (600° to 750 °C) (Christiansen et al., 1986). Magmatic phases include sanidine, plagioclase,
133 quartz, and Fe-rich biotite. Accessory phases include allanite, fluorite, zircon, apatite, ilmenite,
134 and magnetite (Christiansen et al., 1983; Christiansen et al., 2007). Topaz rhyolite often contain
135 vapor-phase topaz, fluorite, bixbyite, pseudobrookite, garnet, and hematite within their
136 devitrified groundmasses or in small vugs; red beryl is a rare but distinctive secondary mineral
137 (Christiansen et al., 1986; Christiansen et al., 1997). In comparison to other topaz rhyolites,
138 which are highly differentiated and rich in incompatible trace elements such as Li, Be, Rb, and
139 Nb, the Spor Mountain Formation is even more evolved, as evidenced by the extreme enrichment
140 of Be and other incompatible trace elements.

141 The beryllium mineralization at Spor Mountain is restricted to the upper part of the
142 highly altered tuff, which lies directly below the thick rhyolite lava (Lindsey, 1977; Foley et al.,
143 2012). The ore zone is approximately 5 to 15 m thick. The principal ore mineral is bertrandite
144 hosted in feldspathic, zeolitic, and argillic tuff and in opaline/chalcedonic replacements of
145 carbonate lithic inclusions. Bertrandite is microscopic and is accompanied by fluorite, calcite,
146 sericite, Li-smectite, and Mn oxides. Fluorine reaches concentrations of up to 1.5 wt% and Be to
147 0.3 wt% in the altered tuff (Bikun, 1980). The deposit contains about 10 million tons of proven
148 and probable reserves at a grade of 0.27 wt% Be (Foley et al., 2012). Several models have been
149 proposed to explain the mineralization in the beryllium tuff. Lindsey (1977) concluded that

magmatic fluids enriched in fluorine and other lithophile elements flowed from an underlying granitic pluton through fractures in the host rock, penetrated the permeable tuff, and caused crystallization of minerals rich in F, Li, Be, Sn, and W as the fluid interacted with the carbonate clasts and volcanic glass in the tuff. Foley et al. (2012) also found evidence for magmatic fluids in the deposit. Conversely, Burt et al. (1982) proposed that the ore deposits formed as Be, U, F, and other elements were released from rhyolite tuff and lava during devitrification, which were then transported and concentrated in the upper part of the tuff below the less permeable rhyolite by meteoric fluids (groundwater). Bertrandite co-precipitated with fluorite and opaline silica as a result of the interaction between the fluid, the host pyroclasts, and carbonate lithic inclusions. Wood (1992) provided geochemical constraints for this low temperature (100-150°C) and moderate pH (4-6) model of ore deposition. Ludwig et al. (1980) used U-Pb dating to show that opal formed or reequilbrated with fluids over a long time period; dates range from 19 to 8 Ma. This is also consistent with the involvement of low temperature groundwater in mineralization. Initial work on the abundance of Be in melt inclusions in the Spor Mountain rhyolite were used to constrain chemical modeling of ore formation and to estimate the minimum volume of magma required to produce the volcanogenic beryllium deposit (0.135 km^3; Adams et al., 2009; Foley et al., 2012)..

Methods

To understand the origin of the rhyolite and its relationship to mineralization, we studied whole rock, mineral, and glass compositions from the Spor Mountain rhyolite. A suite of samples was collected from open pits in Spor Mountain beryllium mine and natural outcrops in a valley east of Spor Mountain. Six fresh samples of lava were selected for more intensive study; the underlying tuff is too altered to be used to examine magmatic processes. Samples SM-

831and SM-86 were from the Taurus Pit (Mine 2 on Fig. 1), SM-14, SM-35, and SM-37 were from the Blue Chalk Pit (Mine 7 on Fig. 1), and SM-31 was collected from the Roadside Mine (Mine 4 on Fig. 1). Samples SM-14, SM-831, SM-86, SM-31, and SM-35 are all vitrophyric lava, and taken from blocks and lenses at the base of the rhyolite lava flows, whereas SM-37 is devitrified, collected toward the middle of a lava flow.

Whole-rock major and trace element analyses were performed on a Rigaku ZSX Primus II X-ray fluorescence (XRF) spectrometer at Brigham Young University. Trace element were also analyzed by ALS Global (Vancouver, British Columbia) using a combination of fusion with lithium metaborate, acid digestion, ICP-MS, and ICP atomic emission spectrometry (AES). The whole-rock results are summarized in Table 1. A comparison of XRF, ICP-MS, and ICP-AES precision and accuracy can be found in Supplementary Table 1.

Electron microprobe analyses (EMP) of plagioclase, sanidine, biotite, and matrix glass were performed using a Cameca SX-50 electron microprobe at Brigham Young University. For sanidine, plagioclase, and biotite, an accelerating voltage of 15 kV, a beam current of 10 nA, and a beam size of 10 μm were used for measurements. For matrix glass, the two-condition method of Morgan and London (2005) was used to optimize the determination of volatile elements. To analyze Na, Al, Si, and Ca, an accelerating voltage of 15 kV, a beam size of 10 μm, and a beam current of 2 nA was used, counting for 30 s on each element. To analyze the remaining elements (F, Cl, Ti, Fe, Mn, Mg, K, and P), beam conditions were set to an accelerating voltage of 15 kV, a beam size of 10 μm, and a beam current of 10 nA, counting for 20 s on each element. Melt inclusions were found in quartz from both more evolved and less evolved rhyolite, but all melt inclusions had cracks. Major elements in melt inclusions were analyzed using the same two-condition method of Morgan and London (2005) as above. The melt inclusions were glassy and

196 less than 20 μm (and thus too small for analyses by LA-ICP-MS). Estimates of accuracy and
197 precision for the electron microprobe analyses are in Supplementary Table 1.

198 Cathodoluminescence (CL) images of quartz were collected using a Gatan miniCL and a
199 FEI XL30 ESEM FEG scanning electron microscope at Brigham Young University. Images
200 were recorded using a spot size of 6 μm, a tilt of 12-15°, a scan acquisition time of 116 ms/line,
201 and an accelerating voltage of 15 kV.

202 Laser ablation ICP-MS analyses were performed on plagioclase, sanidine, biotite, quartz,
203 and matrix glass from four lava vitrophyres (SM-31, -35, -831, and -86) and one devitrified lava
204 (SM-37). To minimize shattering of quartz grains during ablation, 200 μm thick, polished thin
205 sections were used. Measurements were acquired with a 193 nm excimer PhotonMachines laser
206 coupled to an Agilent quadrupole ICP-MS (7500ce Series) at the University of Utah. Laser
207 settings were 15 kV and 10 Hz repetition rate, yielding a fluence of 7.19 J/cm^2 at 100% beam
208 energy. A spot size of 31 μm was used for plagioclase, sanidine, biotite, and matrix glass and a
209 diameter of 53 μm for quartz (quartz grains required a larger spot size to ablate). Acquisition
210 time for each spot was 20 s. Helium was used as a carrier gas at 1 L/min. NIST 610 functioned as
211 the external standard, and ^{29}Si as the internal standard (using electron microprobe measurements
212 of the same grains). Sample SM-831 was run during each analysis and acted as a secondary
213 standard. Data were reduced using Iolite 2.5 (Paton et al., 2011) for Igor Pro. Whenever possible,
214 three spots were analyzed on each grain and averaged, to account for any heterogeneities.
215 Appendix E compares the average LA-ICP-MS analysis of the NIST 610 glass to the GeoRem
216 certified values. Typical relative standard deviations for trace element concentrations in NIST
217 610 are less than 1.6% (Supplementary Table 1).

218 Whole rock Nd, Sr, and Pb isotopic data were obtained by thermal ionization mass

spectrometry using a Finnigan-MAT6-collector solid source mass spectrometer at the University of Colorado, Boulder using analytical procedures outlined by Farmer et al. (1991).

Geothermobarometry

Even though no zoning could be seen in the feldspars, the analyses closest to the rim were used to calculate temperature immediately before eruption (average compositions give similar temperatures). The pressure was set at 2 kbar based on the experiments of Webster et al. (1989) as expanded on below. For this study, any calculations requiring an H_2O term had H_2O set at 5 wt%, as justified below. Zirconium concentrations in the matrix glass and whole rocks were used for the zircon saturation thermometry. For the Ti-in-quartz thermometers, the activity of TiO_2 in the melt ($aTiO_2$) was calculated using the method developed by Kularatne and Audétat (2014), which involves calculating the TiO_2 solubility as a function of the molar Al/(Na+K) ratio, since TiO_2 solubility increases with melt peraluminosity.

Results

Petrography

Two types of unaltered rhyolite were distinguished by petrography (and geochemistry). In thin section, vitrophyres of the "more evolved" rhyolite have clear matrix glass with ~30% phenocrysts while the "less evolved" type has tannish matrix glass and ~15% phenocrysts. Otherwise, both types have similar textures and phenocryst proportions (Fig. 2)—~40% quartz, ~40% sanidine, ~10% biotite, and ~10% plagioclase. Accessory phases in glass and as inclusions in other minerals, identified with the help of energy dispersive spectrometry (EDS), include fluorite [CaF_2], columbite [$(Fe,Mn)(Nb,Ta)_2O_6$], euxenite [$(Y,REE,Th)(Nb,Ta)_2O_6$], fergusonite [$(Y,Ce,Nd)NbO_4$], monazite [$(Ce, La, Th)PO_4$], thorite [$(Th,U)SiO_4$], and zircon [$ZrSiO_4$], all

241 less than 50 μm in size, with most between 20 and 30 μm. In spite of thorough examination and
242 x-ray mapping with the EMP, no phenocrysts of ilmenite, magnetite, or apatite were identified in
243 the matrix or as inclusions in biotite in the vitrophyres, although they have been reported in other
244 topaz rhyolites (e.g. Christiansen et al., 1983). Matrix glass is mostly clean with few microcrysts
245 (Fig. 2); flow banding, defined by tiny microlites, developed in several vitrophyres.
246 Sanidine grains, on average, are larger than plagioclase grains in the same sample, with
247 sanidine ranging in size from 0.5 to 2 mm and plagioclase generally less than 1.5 mm. Both
248 sanidine and plagioclase are euhedral to subhedral and display little to no alteration. Feldspar
249 grains are generally isolated from one another, although some clumps of sanidine and plagioclase
250 are present. Most feldspars are not zoned, neither optically or chemically. However, a few grains
251 (one or two per sample) display anti-rapakivi textures where sanidine mantles plagioclase. This
252 may be explained by the displacement of the melt composition toward the Ab apex of a Q-Ab-Or
253 ternary as H_2O- and F-content of the residual melt increased during differentiation (Christiansen
254 et al., 1984). Few biotite grains are larger than 1 mm with most between 0.5 and 1 mm. Biotite is
255 generally euhedral in vitrophyric lava (Fig. 2). Quartz grains are mostly larger than sanidine,
256 with some grains up to 4 mm, although most are between 1 and 2 mm (Fig. 2). Quartz is not
257 typically embayed as is so common in other rhyolites (Fig. 3). Minor resorption events are
258 evidenced in some quartz grains and marked by abrupt thinning or truncation of CL imaged
259 growth layers (Fig. 3a). Some quartz phenocrysts have glass inclusions, although all inclusions
260 are intersected by cracks and most have at least some secondary crystallization on the walls.
261 Some melt inclusions clearly formed by healing between quench-grown dendritic extensions
262 (Fig. 3b).
263 The less evolved devitrified lava (represented by SM-37; a member of the phenocryst

poor, less evolved group) has a very fine-grained groundmass of quartz and feldspar. Quartz and feldspar phenocrysts are mostly euhedral to subhedral, although some sanidine phenocrysts are slightly embayed along the edges. The majority of biotite phenocrysts in the devitrified rock have been altered to secondary minerals, predominantly magnetite, with reaction textures found on all grains (Fig. 2). Small grains of secondary biotite are also present in the groundmass. Sprays of vapor-phase topaz also occur in the groundmass of devitrified rocks. Large topaz crystals formed in rare vapor phase cavities in devitrified portions of the lava flow. No Be minerals have yet been identified in the unaltered Spor Mountain rhyolite.

The observed petrographic and inclusion relationships can be used to constrain the pre-eruptive crystallization sequence in the Spor Mountain rhyolite. Sanidine commonly has inclusions of quartz, plagioclase, and biotite, while biotite has inclusions of plagioclase, monazite, and zircon. Although uncommon, some quartz grains have inclusions of biotite and feldspar. It is not uncommon to find different phenocryst minerals with euhedral edges touching each other in glomerocrystic clumps. These characteristics suggest that all of the minerals were co-crystallizing before eruption. This is substantiated by the results of plagioclase-liquid, alkali feldspar-liquid, two-feldspar, and Ti-in-quartz thermometry and trace element models outlined below.

The idea that the major minerals were co-crystallizing is also apparent when looking at the two types of rhyolite lava—phenocryst-poor and phenocryst-rich. If the minerals followed a crystallization sequence during differentiation, the less evolved rhyolite could have a different mineral assemblage than the more evolved rhyolite; this is not the case. Both the more evolved and less evolved types have the same mineral assemblage and mineral proportions; the only difference is that the more evolved rhyolites have higher crystallinity.

Whole rock and glass geochemistry

The Spor Mountain rhyolite is a high-silica, high-F, topaz rhyolite (Christiansen et al., 1984; Fig. 4). Compared to other subalkalic obsidians (Macdonald et al., 1992), the Spor Mountain rhyolite is enriched in Be and other rare elements as well as the halogens. It is metaluminous to slightly peraluminous and has very low concentrations of compatible elements, such as Ti, Fe, Mg, Ni, Ca, Eu, Sr, Ba, and P (Table 1). Compared to most other topaz rhyolites, Spor Mountain has lower concentrations of SiO_2 and TiO_2, but higher Al_2O_3 and Fe_2O_3 concentrations and higher contents of incompatible elements (e.g. Christiansen et al., 1983). In these regards, the Spor Mountain rhyolites are similar to the highly evolved rhyolites from the Honeycomb Hills of western Utah, which have phenocrystic topaz (Congdon and Nash, 1991; Byrd and Nash, 1993). Although no Be minerals have been identified in the fresh igneous rocks studied here, the whole-rocks are enriched in Be. With up to 75 ppm Be, the Spor Mountain rhyolite glass contains almost 25 times as much Be as average continental crust (Rudnick and Gao, 2014). The Spor Mountain rhyolite is also enriched in other rare elements compared to average continental crust, such as Li (9 times), Sn (21 times), Nb (12 times), Ta (42 times), and U (13 times). Moreover, it is much more differentiated than typical rhyolites as represented by the obsidians studied by Macdonald et al. (1992; Fig. 4)

Geochemical differences are apparent within the Spor Mountain rhyolites: a more evolved (ME) phenocryst-rich type (SM-14, -831, and -86) and a less evolved phenocryst-poor (LE) type (SM-31, -35, and -37), which has higher concentrations of compatible elements (Mg, Ca, Ti, P, Sc, Ni, Cu, Zn, Sr, Y, Zr, La, Ce, Nd, Sm, Eu, Pb, Th, and U) than the more evolved group (Table 1). Compatibility is defined by negative correlations with decidedly incompatible elements, e.g., Be, Rb, and Nb (see below). Many of these elements (e.g., Y, REE, Th, U) do not

behave compatibly in other magmas, but small proportions of accessory minerals (fluorite, columbite, euxenite, fergusonite, monazite, thorite, and zircon) change their behavior in this system. The silica content of the less evolved vitrophyres ranges from 75.0 to 75.4 wt% (normalized to 100% on a volatile-free basis) and $Na_2O + K_2O$ lies between 8.4 and 9.4 wt% while the more evolved samples have slightly lower silica, ranging from 73.9 to 74.5 wt% SiO_2 and higher alkalies at 9.7 to 10.0 wt% $Na_2O + K_2O$ (Fig. 4). Compared to the more evolved matrix glasses, those from the less evolved glasses also have lower concentrations of incompatible elements, such as Li, Be, Rb, Nb, and Ta (Table 2). For example, Be is almost 2 times and Rb is nearly 1.5 times lower in the less evolved rocks than in the more evolved rhyolite. The less evolved devitrified sample has higher SiO_2 than the more evolved (75.5 wt%), although $Na_2O + K_2O$ (9.0 wt%) is within analytical uncertainty of the other less evolved samples. The lower silica content of the more evolved samples is probably a result of the higher F-content of the melt (1.56 wt% in the more evolved vs. 0.68 wt% in the less evolved matrix glass) and the shift of the ternary minimum toward the albite apex (Manning, 1981; Christiansen et al., 1984; Webster et al., 1987). Fluorine expands the stability field of quartz in granite systems and moves the eutectic toward albite.

As compared to the whole rock composition, matrix glass has lower SiO_2, TiO_2, FeO, and CaO, but higher concentrations of Al_2O_3, Na_2O, and F (Table 2). The glass also has lower Ba, REE, Pb, Sr, Y, and Zr, but higher Be, Cs, Rb, Sn, and Ta, compared to the whole-rocks (Table 2 and Fig. 5). This is consistent with the presence of phenocrysts of feldspar, euxenite, fergusonite, and zircon, along with glass in the whole-rock analyses and points to the role of

crystal separation in the evolving system.

Whole-rock REE patterns for the Spor Mountain rhyolite have relatively low La/Yb ratios compared to other rhyolites, along with prominent negative Eu anomalies and flat heavy REE patterns (Fig. 5a). Such REE patterns are common in other topaz rhyolites (Christiansen et al., 1984). In spite of the F-enrichment, we see no evidence for the tetrad effect (segmentation of a REE pattern into four parts and often attributed to the selective formation of REE-F-complexes; cf. Irber, 1999).

Normalized trace element patterns for the Spor Mountain whole-rocks and matrix glasses reveal strong enrichments in Rb, Th, and Nb and large negative Ba, Sr, and Eu anomalies and that are deeper in the more evolved rocks/glasses (Fig. 5), consistent with feldspar fractionation. More evolved matrix glass shows greater depletion in REE and incompatible elements than matrix glass from less evolved samples.

Considering the role of highly differentiated magma in the development of economic deposits of rare metals, the concentrations of many elements in the Spor Mountain rhyolites are remarkably high, with Be (40-75 ppm), B (100-200 ppm), Sn (30-50 ppm), and W (20-40 ppm). For example, the highly evolved Hideaway Park tuff, which is related to the Henderson porphyry molybdenum deposit, has significantly lower concentrations of these incompatible elements (as much as 5 times), i.e., Be (8-16 ppm), B (36-39 ppm), Sn (9-10 ppm), and W (9 ppm) (Mercer et al., 2015). On the other hand, the Hideaway Park tuff is strongly enriched in Mo (4-15 ppm vs 2 ppm in Spor Mountain glass. Audetat (2015) and Audetat and Li (2017), using melt inclusion data, summarize evidence for much higher concentrations of Mo in rhyolites associated with porphyry molybdenum deposits. They found from 4-20 ppm Mo at comparable Cs or Rb concentrations, which were used as an indicators of melt fractionation. Another contrast between

354 the Hideaway Park and the Spor Mountain rhyolites lies in the extremely high Li contents in the
355 Hideaway Park melt inclusions (1600-3700 ppm); its glass matrix has only ~70 ppm. The Spor
356 Mountain rhyolite also has 75-100 ppm Li in the matrix glass.

357 **Melt inclusion geochemistry**

358 Quartz-hosted melt inclusions were analyzed by EMP in thin section of one less evolved
359 and three more evolved rhyolites (Supplementary Table 2). We analyzed only inclusions that
360 lacked alteration or evidence of pervasive secondary crystallization. At Spor Mountain,
361 differences between the compositions of the melt inclusions and the matrix glass in the same
362 sample are small. For the inclusions in the more evolved rocks, the melt inclusions have higher
363 K_2O (5.16-6.22 wt% vs 4.60-5.09 wt%) and lower CaO (0.07-0.15 vs. 0.3-0.5 wt%), and
364 Fe_2O_{3Total} (0.4-0.9 vs. 0.9-1.4 wt%) than the associated matrix glass. Similar differences are
365 found between melt inclusions and matrix glass in the less evolved rocks. Fluorine
366 concentrations are slightly lower in the melt inclusions from the more evolved samples than in
367 matrix glass (0.70-0.97 wt% vs 1.45-1.65 wt%), but Cl, an even more volatile element, has
368 essentially the same concentration in both matrix glass and in melt inclusions (0.24 to 0.31 wt%
369 in melt inclusions vs 0.20-0.31 wt% in matrix glass; Table 2 and Supplementary Table 2).
370 Furthermore, the melt inclusions in the more evolved rocks are chemically distinct from the less
371 evolved type, with lower concentrations of SiO_2, TiO_2, and CaO and higher Al_2O_3, Na_2O, and
372 K_2O. These trends mimic, for the most part, the differences between the matrix glasses in the
373 two groups and provide confidence that the glass matrix reliably reflects the evolving
374 composition of the pre-eruptive magma. It should be noted, however, that all of the analyzed
375 melt inclusions were intersected by cracks—some could have been induced during sample

preparation—suggesting that the inclusions may have been open at some point allowing volatiles like Cl, F, and perhaps, Be and Li to escape.

Using LA-ICP-MS, Hofstra et al. (2013) have determined Li concentrations in melt inclusions in Qz from the Spor Mountain rhyolite. They concluded that melt inclusions from Spor Mountain have the highest known Li concentrations (max 5,200 ppm, median 3,750 ppm) compared to matrix glass concentration of only ~70 ppm. If melt inclusions accurately preserve magmatic concentrations of volatile elements like Li, then our data support the conclusion of Hofstra et al. (2013) that much (98%) of the Li was lost in vapor during eruption and emplacement of the lavas. However, it is puzzling why Li should be so enriched and other incompatible elements (e.g. Be, B, Rb) are not also enriched to the same extent in the melt inclusions (A. Hofstra, written communication, 2015). Audetat (2015) notes that Li concentrations in quartz-hosted melt inclusions higher than ~100-1500 ppm are caused by diffusive exchange of alkalies through quartz.

Mineral Chemistry

Feldspar. Zoning (optical or chemical) is not apparent in plagioclase or sanidine. Electron microprobe analyses confirm that differences between the two groups of fresh vitrophyres also extends to the mineral compositions (Fig. 6; Supplementary Tables 3 and 4). Plagioclase ($An_8Ab_{80}Or_{12}$ vs $An_5Ab_{86}Or_9$) and sanidine ($An_1Ab_{46}Or_{53}$ vs $An_1Ab_{53}Or_{46}$) are more sodic in the less evolved magma than in the more evolved type. These differences are reconcilable if the less evolved magma was crystallizing at a higher temperature before eruption. The 2 kb solvi at 700°C and 650°C are plotted on Figure 6 for comparison. Feldspars from the less evolved rhyolite typically have lower concentrations of incompatible trace elements such as B, Ga, Cs, and Pb, and higher concentrations of Zn, Sr, and Nb, and Ba (Supplementary Tables 3

399 and 4) compared to those from more evolved lavas. The composition of the phenocrystic feldspar
400 in the devitrified sample clusters near the less evolved group, although there is a larger spread in
401 sanidine compositions (between $An_1Ab_{61}Or_{38}$ and $An_5Ab_{86}Or_9$) as a result of continued
402 crystallization of more sodic sanidine on the rims of grains during devitrification. Microcrystals
403 of sanidine and plagioclase in the groundmass of the devitrified sample are similar in major
404 element composition to the phenocrysts.
405 Sanidine from the highly evolved Bishop Tuff (Hildreth, 1979) from eastern California is
406 generally more potassic than Spor Mountain sanidine (between Or_{60} and Or_{70}; Fig. 6), and
407 plagioclase is more calcic (between An_{20} and An_{30}), consistent with higher temperatures of
408 equilibration (Fig. 6). Plagioclase from the topaz rhyolite at Honeycomb Hills, Utah (Congdon
409 and Nash, 1991) is similar to plagioclase in the more evolved Spor Mountain rhyolite, with a few
410 being nearly An_2, although the sanidine grains are noticeably less sodic, plotting instead near the
411 Bishop Tuff (Fig. 6). Moreover, Ba concentrations in sanidine and plagioclase in the Honeycomb
412 Hills rhyolite (20 ppm) are similar to those in the Spor Mountain rhyolite (25 ppm) (Congdon
413 and Nash, 1991).
414 **Biotite**. All vitrophyres contain unaltered biotite (~10% of the phenocrysts). About 25%
415 of the biotite grains contain accessory minerals (~80% zircon and euxenite, with lesser amounts
416 fergusonite, columbite, thorite, and monazite, based on EDS analysis), and those that do contain
417 accessory minerals often contain more than one mineral phase. Zircon inclusions are generally
418 euhedral, while other minerals are subhedral to euhedral. The inclusions appear in both the rims
419 and the cores of biotite grains.
420 Biotite from the Spor Mountain rhyolite is extremely Fe-rich, with Fe/(Fe+Mg) ratios

421 >0.95, and F-rich (1.6 to 2.6 wt%). The biotite compositions fall within the field of A-type
422 granites as defined by Christiansen et al. (1986). The high Fe/Mg ratios are probably related to
423 relatively low fO_2, but quantitative estimates are hindered by the lack of a coexisting Fe-Ti
424 oxides. Biotite from the less evolved rhyolite contains higher TiO_2 and MgO and less Al_2O_3 and
425 F and lower concentrations of incompatible Li, Ga, and Nb than more evolved ones (Fig. 7;
426 Supplementary Table 5).
427 Compared to biotite from the Bishop Tuff (Hildreth, 1979), magmatic biotite from Spor
428 Mountain has higher Fe/(Fe+Mg) ratios and Al apfu (Fig. 7). The Spor Mountain biotite also has
429 considerably more F than the Bishop Tuff (as high as 2.6 wt% in Spor Mountain vs ~0.51 wt% in
430 the Bishop Tuff). However, biotite from the Honeycomb Hills tends to have even higher Al apfu,
431 although with similar Fe/(Fe+Mg) and F as Spor Mountain biotite (Congdon and Nash, 1991).
432 Although Fe-rich, the biotite is not Li-rich zinnwaldite like that in some mineralized systems; it
433 has only 350 to 1000 ppm Li. For example, zinnwaldite found in the topaz-bearing Sheeprock
434 Granite (Rogers, 1990) of western Utah has more SiO_2, Al_2O_3, MnO, MgO, K_2O, and F and less
435 TiO_2, FeO, Na_2O, and Cl, compared to the biotite in the Spor Mountain rhyolite.
436 Because of Fe-F avoidance (Ekstroem, 1972), the F content of biotite of differing Mg/Fe
437 ratio is not a good indicator of the magnitude of F enrichment. To eliminate this problem, Munoz
438 (1984) defined a F-intercept value [IV(F)] which is the logarithm of the ratio of the fugacities of
439 H_20 and HF at infinite temperature. He formulated a similar intercept value for Cl [IV(Cl)]. The
440 smaller the intercept value for a particular biotite, the higher the degree of halogen enrichment in
441 the magma it crystallized from. IV(F) for Spor Mountain rhyolite range from 0.74 to 0.89 in the
442 less evolved samples and 0.57 to 0.66 in the more evolved rhyolite (Supplementary Table 5). The

IV(Cl) values range from ~-4.0 for biotite in the less evolved rhyolite to -3.9 in the more evolved rhyolite. Thus, biotite compositions show that fugacities of F and Cl were lower in the less evolved melt compared to the more evolved melt, as expected from the elemental concentrations of F and Cl in the glasses.. Moreover, the halogen fugacities in the Spor Mountain rhyolite are more similar to those of porphyry Mo deposits than to Cl-rich porphyry copper deposits or even to Sn-W-Be deposits as compiled by Munoz (1984).

Devitrified samples contain highly altered biotite grains with magnetite along cleavage planes. As expected, the altered parts of the phenocrystic biotite also have lower Fe, as the Fe was mobilized into the oxides, and lower Fe/(Fe+Mg). They also have with higher F contents, although TiO_2 is similar to phenocrystic biotite (Fig. 7; Supplementary Table 5). Another type of secondary biotite formed in the groundmass of some devitrified rocks. It has less TiO_2 and more MgO, Al_2O_3, F, and Cl than the phenocrystic biotite in the vitrophyres, and it has a lower and more variable Fe/(Fe+Mg) ratio (Supplementary Table 5; Fig. 7). The trace element composition of the secondary biotite is also distinct from the magmatic biotite. Biotite in the devitrified sample contains higher Li, Be, B, Ga, Rb, Zr, Nb, Mo, Sn, REE, Cs, Ta, W, and Pb compared to magmatic biotite in the less evolved vitrophyres (Supplementary Table 5). Similarly, the devitrified rocks have significantly more Li and B in sanidine (22 ppm Li; 174 ppm B) and plagioclase (54 ppm Li; 150 ppm B) compared to sanidine (11 ppm Li; 69 ppm B) and plagioclase (30 ppm Li; 64 ppm B) in the vitrophyres. Thus, devitrification mobilizes Li and perturbs the original composition of phenocrystic phases as they attempt to equilibrate with vapors released during crystallization of the glass/melt.

Quartz. Cathodoluminescence images show that the majority of quartz grains have thin

oscillatory light and dark growth bands (Fig. 3), a function of differences in trace element concentrations related to kinetic effects, pressure changes, or temperature oscillations (Rusk et al., 2006; Rusk, 2012; Frelinger et al., 2015). Many grains also show signs of resorption episodes (Fig. 3b) during their crystallization histories in the form of shallow embayments and abrupt terminations of individual zones. Furthermore, some grains display evidence of rapid growth (dendritic extensions on corners) followed by infilling, as seen in Figure 3b. However, most grains are euhedral and new crystal growth appears on the rims of most grains, indicating that the final stage prior to eruption was quartz growth.

Less evolved samples contain quartz with higher Ti, P, and Fe than the more evolved samples, with Li, B, and Al displaying no consistent differences between the two groups (Supplementary Table 6). Compared to the Bishop Tuff (Anderson et al., 2000), Spor Mountain quartz has considerably less Ti (~30 ppm in Spor Mountain vs ≥450 ppm in Bishop Tuff quartz) and Fe (~78 ppm in Spor Mountain vs ≥3500 ppm in the Bishop Tuff), probably as a result of lower temperatures and more evolved melt compositions. Compared to quartz in other silicic magmas (Liu et al., 2006; Breiter et al., 2012), quartz from the Spor Mountain rhyolite has higher concentrations of Li, B, and Al.

Thermometric Summary. The majority of geothermometers converge on a temperature of ~700 °C for an average of the less evolved and more evolved rhyolites, including the zircon saturation, alkali feldspar-liquid, two-feldspar, and the Ti-in-quartz thermometers (Table 3). However, the TitaniQ equation of Thomas et al. (2010) gives anomalously low temperatures, below 560 °C at 2 kb (Table 3). To produce a Ti-in-quartz temperature of 700 °C, an unreasonably high P of ~8-12 kb would have to be used, pressures that are inconsistent with the experimental phase equilibria (Webster et al., 1987). Given the agreement of the other thermometers at ~700 °C, it seems that this thermometer is not useful for this system. The biotite thermometer by Righter and Carmichael (1996) gives the opposite result, in that it returns temperatures that are too high (all temperatures are above 780°C). For more detailed discussion see Dailey (2016).

In detail, the less evolved rhyolite was slightly hotter (~20-30°) than the more evolved rhyolite in all of the thermometers except TitaniQ where the temperatures were statistically indistinguishable.

Partition coefficients

Mineral-liquid partition coefficients were calculated using LA-ICP-MS data for rims of sanidine, plagioclase, biotite, quartz, and matrix glass and are summarized in Table 4 and Figures 8 and 9. Sanidine and plagioclase partition coefficients are similar, with the notable exceptions of Ba and Pb, both of which are more compatible in sanidine. Partition coefficients for each mineral in both compositional types are similar. For example, the partition coefficient for Rb in sanidine is 0.44 in the less evolved rhyolite and 0.36 in the more evolved rhyolite; the difference is within the analytical uncertainty of ± 0.08 ppm. Because of mineral-structure controls, biotite has much higher partition coefficients for Mn, Ti, Mg, Zn, Li, and Rb than the feldspars and quartz.

The Spor Mountain rhyolite has high F (up to 1.7 wt% F in glass), which, like water, acts as a network modifier, depolymerizing melt structures (Genson et al., 2007; Bartels et al., 2013), thus lowering mineral-melt partition coefficients (e.g. Hall, 1957). On the other hand, temperature is an important control on both viscosity and partition coefficients. The competing effects of these two parameters are seen in the F-rich, but low temperature Spor Mountain rhyolite.

Using the measured partition coefficients, Onuma diagrams (Onuma et al., 1968) were constructed for sanidine, plagioclase, and biotite (Fig. 10). Partition coefficients for each element, arranged by coordination-dependent ionic radius, were plotted and lines were drawn to signify the optimal ionic radius for each crystallographic site (i.e., the T-, M-, and I-sites for biotite, and T- and M-sites for sanidine and plagioclase). Such diagrams provide an elegant explanation of why each element behaves the way it does. For example, Sr partitions strongly (D~6) into the M-site of plagioclase because it has the right size and charge. Lead, which has a similar size but lower charge, partitions only weakly (D~1) into that site. Metallogenetically important elements like Sn, W, and Mo have low partition coefficients in the rhyolite and should behave incompatibly. Tin partitions weakly in feldspars but more strongly in biotite (D~0.9) because its size allows it to fit in the M-site. Tungsten is incompatible in all three silicates examined here (D<0.1); partition coefficients are similar to those of other highly charged ions (e.g., Zr, Hf, Nb, Ta). Molybdenum is strongly incompatible in feldspars (generally below detection) but more compatible in biotite (D~1) where it appears to behave like Al. Of particular note is the predicted location of Be^{+2} within the minerals; instead of substituting in M-sites for Li^{+1}, Na^{+1}, or Mg^{+2} which are near Be on the periodic table, Be substitutes for Si^{4+} in the T-site. This conclusion is consistent with Ryan's (2002) observations of Be partitioning in

527 plagioclase and pyroxene.

528 Partition coefficients for most elements in Spor Mountain sanidine and plagioclase are
529 comparable to other silicic magmas (Mahood and Hildreth, 1983; Nash and Crecraft, 1985;
530 Congdon and Nash, 1991; Figure 9). Biotite partition coefficients for Zn, Rb, Zr, Cs, Th, and the
531 light REE are between two and five times lower than in other highly evolved rhyolites. The
532 higher partition coefficients for biotite of the Twin Peaks (Nash and Crecraft, 1985) and Bishop
533 Tuff (Mahood and Hildreth, 1983) can be explained by the presence of inclusions in the biotite
534 as they were measured using mineral separates, not in situ LA analyses of individual mineral
535 grains. Finally, quartz partition coefficients are comparable to partition coefficients measured in
536 other magmas, although D_{Al} in quartz in Spor Mountain samples is slightly lower (Fig. 9).

537 The behavior of Be is of particular importance for this study, so it is important to
538 compare our Be partition coefficients with those derived by others (Fig. 11). Several other
539 studies of highly evolved rhyolites have reported mineral/melt partition coefficients for Be (e.g.
540 Kovalenko et al., 1977; Evensen et al., 1999; Evensen and London, 2002). Kovalenko et al.
541 (1977) measured Be partitioning between phenocrysts and devitrified groundmass in F-rich
542 ongonites using mineral separates. (Ongonites are highly differentiated topaz-bearing dike rocks
543 related to rare metal granites.) They report much higher Be partition coefficients than we
544 measured for the Spor Mountain rhyolite, but that could be the result of Be-loss from the
545 ongonite groundmass during devitrification. In fact, Be concentrations in the ongonite
546 groundmass are typically much lower (18 ±18 ppm) than in the Spor Mountain glass (45-75
547 ppm). Beryllium concentrations in the Spor Mountain feldspars are similar to those in the
548 ongonites. Another complication with the ongonite data, might be caused by inclusions of tiny
549 Be-rich phases in the feldspar separates. Kovalenko et al. (1977) report much higher

concentrations of Be in what they call "mica," but the composition of the mica in the ongonites is not given. Biotite, muscovite, and Li-phengite have been reported from these dikes and Be should behave very differently in biotite than it does in the other phases. Moreover, it is not clear that the mica is magmatic rather than hydrothermal. Thus, comparison with ongonites is problematic. Evensen and London (2002) measured Be partition coefficients in experiments with hydrous granitic melts. In Be-poor rhyolitic melt (<25 ppm Be), the partition coefficients for Be in sodic plagioclase are similar to those we measured (D_{Be}=0.11 vs. 0.17 measured here), but partition coefficients for sanidine (D_{Be}=0.19 to 0.38 vs. 0.05), biotite (D_{Be}=0.39 to 0.54 vs. 0.04), and quartz (D_{Be}=0.24 vs. < 0.04 [Be was not detected in Spor Mountain quartz]) are much higher than those for the Spor Mountain rhyolite. They also concluded that Be was compatible in oligoclase (D_{Be}=1.8) and in muscovite (D_{Be}= 1.35)—phases not stable in the Spor Mountain magma—and that Be partition coefficients increased at low temperature like those of the Spor Mountain rhyolite. However, in Be-rich melt (>130 ppm Be and saturated with beryl or phenakite), Evensen et al. (1999) found Be partition coefficients were lower and more similar to those we measured: sodic plagioclase (D_{Be}= 0.37 vs. 0.17), sanidine (D_{Be}=0.14 to 0.18 vs. 0.05), and biotite (D_{Be}=0.08 vs 0.04). Some of the differences might be related to the water-saturated and F-poor character of the experiments; Be may have partitioned preferentially into the fluid.

Isotopes

Strontium, Nd, and Pb isotopic compositions of two samples of the less evolved rhyolite (SM-31 and SM-35) and two samples of Sheeprock Granite are reported in Table 5 and Figure 12. The Sheeprock Granite is included here because it is so similar to the Spor Mountain rhyolite

in location, age, composition, and mineralogy and provides additional information about the genesis of Be-rich magma. εNd_t values (corrected to 21 Ma) are -7.2 and -7.8 for the Spor Mountain rhyolite and slightly higher for the Sheeprock Granite (-5.9 and -6.3). Due to the low Sr and high Rb concentrations, $^{87}Sr/^{86}Sr_i$ values are very sensitive to the age used in making corrections to initial values and are not reported for the Spor Mountain rhyolite. So the $^{87}Sr/^{86}Sr_i$ (0.7064 ± 0.0002) of the 21 Ma Sheeprock Granite, derived from a whole-rock Rb-Sr isochron (Christiansen et al., 1988), is used as a proxy for the Sr-isotopic composition of the Spor Mountain rhyolite.

Discussion

In the following paragraphs, we outline the general constraints on the physical parameters (temperature, pressure, water content, and viscosity) that prevailed before eruption of the Spor Mountain rhyolite. These are then used, along with trace element and isotope geochemistry, to construct a model for the origin and evolution of the rhyolite, identifying the key factors for the generation of high Be content, which ultimately was a fundamental control on the origin of the Be ore deposits.

Pre-eruptive temperature, pressure, water content, and viscosity

Ti-in-quartz thermometry and barometry. In spite of the higher Ti content in less evolved quartz (25 ppm vs 16 ppm), the temperatures calculated for the less evolved magma were lower than more evolved magma, contrary to other thermometers. However, the temperature differences are small and within the uncertainties of the method. Slightly different activities of TiO_2 and pressure cause significant temperature differences. An increase in $a TiO_2$ of 0.10 (the uncertainties of our calculations) results in ~39°C lower temperatures using Huang

593 and Audétat (2012) and ~30 °C lower temperature using Thomas et al. (2010). Conversely, an
594 increase in 1 kbar results in ~32 °C higher temperatures using Huang and Audétat (2012) and
595 ~22 °C higher temperatures using Thomas et al. (2010). Therefore, quartz in the less evolved
596 rhyolite could have crystallized at a higher pressure than quartz in the more evolved rhyolite.
597 However, the estimated pressure differences are quite large—the less evolved rhyolite would
598 have been under 1–2 kbar more pressure, or roughly 3 – 8 km deeper. This depth difference
599 seems too large, given the small volume of rhyolite erupted. Thus, we suggest that small errors in
600 the calculated value of $a\mathrm{TiO_2}$, probably account for the apparent temperature inversion.

601 Based on CL images (Fig. 3; supplementary file B), the quartz grains have oscillatory
602 zonation. Although oscillation widths are generally smaller than the diameter of the laser spots,
603 Figure 3a shows a thick bright zone that is nearly the same size (~60 μm) as the laser beam (53
604 μm). This zone has 2 or 3 ppm higher Ti than adjacent darker zones; this Ti difference
605 corresponds to a temperature difference of 2 or 3°C, all else being equal. Thus, only minor
606 changes in temperature are needed to create the oscillatory zoning seen in CL, assuming a
607 constant pressure of 2 kb. Assuming a constant temperature of 700°C, a difference of only 0.1
608 kb, using Huang and Audétat (2012) P-T sensitive calibration could cause the observed Ti
609 concentration differences. Thus, it seems possible that small oscillations in temperature or
610 pressure in a convecting magma could cause these small variations and produce the zoning seen
611 in the quartz. More likely causes, however, were kinetics, which affect the delivery of Ti to the
612 crystal-liquid interface. Short episodes of more rapid growth could cause buildup of
613 incompatible Ti at the crystal-liquid interface which is then incorporated into the next growth
614 step. Bacon and Druitt (1988) demonstrated this effect for $\mathrm{P_2O_5}$ near growing crystals in the

615 dacite erupted from Mt. Mazama. The extremely slow diffusion rate for Ti in quartz allowed the
616 delicate oscillatory zonation to be preserved (Fig. 3).

617 **Pressure.** Using the phase diagram produced by Webster et al. (1987) for Spor Mountain
618 rhyolite, it is possible to constrain the pressure at which the minerals crystallized within the Spor
619 Mountain magma. Based on the conditions necessary for all of the main phases to be present, the
620 minerals would have needed to crystallize around 2 kb (Fig. 13). Furthermore, the majority of
621 geothermometers converge on ~700 °C, when assuming a pressure of 2 kbar.
622 To estimate the pressure of crystallization, temperatures were calculated for the various
623 thermobarometers over a range of pressures and then plotted together (Fig. 14). Those that are
624 heavily influenced by pressure have steep slopes, whereas thermometers that are not P-sensitive
625 have no slope (vertical line). The intersections of the P-T curves provide estimates of the
626 pressure at which the Spor Mountain rhyolite crystallized. For the less evolved sample (SM-31),
627 most pressure-sensitive thermobarometers cross between 1.5 and 2.5 kbar and ~700 °C. For the
628 more evolved samples (SM-831), the pressure at which the curves cross is a bit lower, between 1
629 and 2 kbar and between 650 and 700°C. Thus, a pressure of 2 kbar seems to be a good estimate.
630 In contrast, the Thomas et al. (2010) calibration of Ti-in-quartz yields extremely high pressures
631 (more than 8 kbar) for any reasonable temperatures.

632 **Water content.** The water content of magma is an extremely important but hard to
633 quantify parameter. In an experimental study, Webster et al. (1987) estimated that the pre-
634 eruptive water content of the Spor Mountain magma had a lower limit of 4 wt%, but was more
635 likely 5 wt%. According to the 2 kbar phase diagram constructed by Webster et al. (1987; Fig.
636 13), the observed phenocryst phases could only be stable at temperatures under ~725 °C with 4-5
637 wt% H_2O in the melt. If water contents were higher, feldspars and quartz would not have been

638 stable and only biotite would have been present at the low temperature. Moreover, according to
639 these experiments the Spor Mountain magma appears to have been water-undersaturated. If all
640 three felsic phases were present in a water-saturated magma of Spor Mountain composition, the
641 temperature would have to have been less than about 600°C. Thus, for the purposes of this study,
642 the pre-eruptive water content for both the more evolved and less evolved melts is assumed to be
643 5 wt%.

644 **Viscosity.** The viscosity of the Spor Mountain rhyolite melt was calculated using the
645 equation of Giordano et al. (2008) which includes the effects of F and H_2O. Assuming 5% H_2O,
646 a temperature of 700°C, a pressure of 2 kb, and a F content reported in Table 2, this model gives
647 viscosities of ~$10^{5.8}$ Pa·s for the more evolved rhyolite and ~$10^{6.2}$ Pa·s for the less evolved
648 rhyolite. A temperature increase of 20°C to 720°C results in the same viscosity reduction as the
649 addition of an extra 1.6% F. Thus, the effects of even large amounts of F in reducing viscosity
650 (Manning, 1981) are not as dramatic as "small" temperature differences. Mercer et al. (2015)
651 estimated the viscosity of the Hideaway Park Rhyolite at ~$10^{4.9}$ Pa s—using 0.95% F and 5.8%
652 H_2O; the lower viscosity is a function of the higher temperature (750°C) they assumed. Another
653 point of interest is that, despite the higher temperatures, the less evolved Spor Mountain melt had
654 a higher viscosity (~$10^{6.2}$ Pa·s) than the more evolved melt (~$10^{5.8}$ Pa·s), a result of the higher
655 silica and lower F content in the less evolved melt. However, when the Einstein-Roscoe (Marsh,
656 1981) equation is applied to these samples, the additional phenocrysts in the more evolved
657 samples causes the more evolved magma to have a higher viscosity (Supplementary Table 7).

658 **Petrogenesis of the Spor Mountain Rhyolite**

659 Based on the elemental and isotopic composition of the Spor Mountain rhyolite, we can

outline a general model for its origin and subsequent evolution. First, we consider what processes formed the observed chemical variety in the rhyolite (how it evolved) and second, we describe its petrogenesis.

Incremental assembly. It is possible that the chemical variation in some magma bodies is the result of accumulating multiple batches of melt formed by different degrees of melting of a common source. To test the role of this process in establishing the compositions of the Spor Mountain rhyolite, we use variations in the compatible elements. Large ranges in concentrations of compatible elements cannot be produced by batch partial melting of a single source, as the range is limited by $\mathbf{1/\bar{D}}$ (Shaw, 1970; Hanson, 1978). Equation 1 is used to model the role of incremental growth of the Spor Mountain magma by accumulation of separate magma batches formed by different degrees of melting:

$$C_L = C_O f^{\bar{D}-1} \frac{C_o}{\bar{D} + f(1-\bar{D})} \quad (1)$$

where C_o, C_L, $\overline{D}$, and *f* are the original concentration of an element in the feldspar-bearing crustal source the concentration in the liquid, the measured bulk partition coefficient, and the fraction of melt extracted in a single batch, respectively. Figure 15 shows the contrasting results of the two processes on Zr/Zr^o and Y/Y^o, relative to Be^o/Be, where X is the elemental concentration in the more evolved rhyolite and X^o is the elemental concentration in the less evolved rhyolite. Because of beryllium's strong incompatibility, Be^o/Be can be used as a proxy for *f*—the fraction of melt. Depletions in the compatible elements are significantly larger than predicted by batch partial melting. Apparently, variable degrees of partial melting cannot account for the differences between the more evolved and less evolved Spor Mountain magmas, even though ultimately partial melting must have been important in forming the original magma, as

681 shown below.

682 **Evolution by fractional crystallization.** To test whether the elemental variations in the
683 Spor Mountain rhyolite could result from crystal fractionation, we have calculated how much
684 crystal fractionation would be needed to get from the less evolved to the more evolved magma.
685 This was accomplished by using the inverse modeling approach developed by Allegre et al.
686 (1977), as summarized below.

687 Concentrations of each trace element in glass analyzed by LA-ICP-MS were plotted
688 against Be to create trace element variation diagrams (Fig. 16). Beryllium was chosen as the
689 index element because (1) it shows the strongest enrichment from less evolved to more evolved
690 rhyolite and thus appears to have the lowest bulk partition coefficient, (2) it varies uniformly in
691 all samples, and (3) it is an element of interest. This choice is also justified with the measured
692 partition coefficients (Fig. 9; Table 4); using the estimated modal abundances and the measured
693 D's, the calculated bulk D for Be is ~0.06. The bulk partition coefficient can then be used to
694 calculate *f*, the fraction of residual liquid in the differentiating magma. During ideal
695 fractionation, the Rayleigh fractionation law (Neumann et al., 1954) describes the trace element
696 concentrations in residual liquids (C_L), relative to a parental melt (C_o):

$$C_L = C_O f^{\overline{D}-1} \quad (2)$$

697 where $\overline{D}$ is the bulk partition coefficient. If $\overline{D} << 1$, the element (denoted C*) is highly
698 incompatible in the melt and the following is true:

$$C_L^i = \left(\frac{C_O^*}{f}\right) or\ f = \left(\frac{C_O^*}{C_L^i}\right) \quad (3)$$

699

700 Thus, a highly incompatible element can serve as an indicator of the degree of differentiation

within a magmatic system. Substituting equation 3 into equation 2 removes *f*, allowing the Rayleigh law to be expressed in terms of relative concentrations of two elements:

$$C_L = C_O \left(\frac{C_O^*}{C_L^*}\right)\left(\overline{D} - 1\right) \quad (4)$$

which, written in the logarithmic, is:

$$\ln C_L = \ln C_O + \left(1 - \overline{D}\right) \ln \left(\frac{C_L^*}{C_O^*}\right) \quad (5)$$

In this linear equation, assuming $\overline{D}$ remains constant throughout the fractionation process, $(1 - \overline{D})$ is equal to the slope of the line on a logarithmic variation diagram of Be versus an element of interest. Thus, the $\overline{D}$ for any element can be calculated from

$$\overline{D} = 1 - m \quad (6)$$

where m is the slope of the line. With the $\overline{D}$ known, it is possible to calculate *f* for each sample by rearranging equation 2 to get

$$f = \left(\frac{C_L}{C_O}\right)^{\frac{1}{\overline{D}-1}} \quad (7)$$

The results of these calculations, along with concentrations C_L and C_O, are summarized in Table 6. Bulk partition coefficients range to as high as 3.9 for Y, more than 3.0 for MREE, and 2.7 for Sr. We find no evidence for enhanced incompatibility of HFSE as predicted for F-rich melts by Keppler (1993); Zr, Hf, Th, and REE are all strongly compatible and largely controlled by accessory minerals enriched in these elements. Moreover, Nb ($\overline{D}$ =0.7) and especially Ta ($\overline{D}$ =0.08) are incompatible.

From the calculations, it also appears that the most evolved melts represent an *f* of 0.55 to 0.60 relative to the less evolved rhyolite (Table 6). However, as the less evolved rhyolite is not the parental primary melt, this is a minimum estimate for the total amount of fractionation from

some more mafic parent, as described below.

Another way to test the accuracy of the inverse modeling method is by using the measured partition coefficients to calculate the weight fractions of the minerals within the sample, using equation 8.

$$\overline{D^i} = D^i_{a/L}X_a + D^i_{b/L}X_b + \cdots \quad (8)$$

where $D^i_{a/L}$ is the partition coefficient of element i between phase a and liquid L and X_a is the weight fraction of the phase in the mineral assemblage. Thus, an equation can be written for each element. This set of equations can be solved simultaneously to calculate the proportions of the minerals involved in the fractionation process. Solving for the proportions of accessory minerals was not feasible as partition coefficients for key mineral phases (euxenite, fergusonite, and thorite) are lacking. Thus, we did not use trace elements that were strongly controlled by accessory minerals. The calculated weight fractions of the major minerals are similar to what is observed optically with a petrographic microscope—40% quartz, 40% sanidine, 10% biotite, and 10% plagioclase. This shows that the calculated $\overline{D}$'s and associated crystal fractionation calculations are internally consistent.

Using the same method, Christiansen et al. (1984) concluded that 75% crystallization was needed to explain the variation in younger Topaz Mountain Rhyolite. Although invoking a complex model of filter pressing, crystal settling, magma recharge, magma mixing, and volatile exsolution to explain a wide range of trace element concentrations, Mercer et al. (2015) also estimated that about 60-70% crystallization could explain the range of Rb and Mo in melt inclusions in the topaz-bearing Hideaway Park Tuff which was related to the Climax-type Mo deposit at Henderson, Colorado.

Thus, based on these trace element models, we conclude that the elemental variations

740 between the less evolved and more evolved Spor Mountain magma can be explained by 40-45%
741 crystallization (f = 0.55-0.60) of the less evolved magma. Moreover, extensive fractional
742 crystallization is called for, even though major element concentrations (especially SiO_2) change
743 very little across the spectrum of compositions.

744 **Magma Origin.** The formation of A-type magmas like the Spor Mountain rhyolite has
745 been attributed to various processes, including fractionation of mantle-derived basalt (e.g.
746 McCurry et al., 2008), partial melting of Proterozoic crust (Christiansen et al., 1986; Christiansen
747 et al., 1988; Ramo and Haapala, 1995; Jacob et al., 2015), partial melting of deep crustal
748 equivalents of peraluminous two-mica granites like some Mesozoic intrusions in the Great Basin
749 (Moore and Sorensen, 1978; Bikun, 1980), or partial melting of crust extensively hybridized with
750 young intrusions of mantle-derived basalt/gabbro (Christiansen et al., 2007). We use isotopic
751 compositions and simple trace element models to distinguish among these possibilities. In Figure
752 12, the Sr and Nd isotopic compositions of the possible sources are compared to the Spor
753 Mountain rhyolite and the geochemically similar Sheeprock Granite. The results of the trace
754 element calculations are shown in Figure 17 and the parameters used in each model are
755 summarized in Table 7. Bulk partition coefficients were based on typical phase assemblages of
756 the different protoliths and mineral/melt partition coefficients from this study. We envision the
757 origin of the rhyolites as a two-fold process; first, batch partial melting of a source, followed by
758 fractional crystallization of that batch of melt in a second stage.

759 First, the isotopic data show that the rhyolite magmas are not simple fractionates of
760 mantle-derived magma. The εNd values for the silicic rocks (-7.8 to -4.8; Fig. 12) are too low for
761 this to be considered seriously; the requisite intermediate magmas are missing in this bimodal
762 suite. Some continental crustal component must be involved as well. Moreover, trace element

763 calculations show that partial melting of the intrusive equivalents of rift-related Miocene basalt
764 does not produce rhyolite similar to that at Spor Mountain. An example of such
765 contemporaneous basalts, are the Miocene alkali basalts from the Nye Canyon area of central
766 Nevada; they have ocean island basalt-like trace element and isotopic characteristics (Farmer et
767 al., 1989). Another example is the 19 Ma Mosida Basalt from central Utah (Christiansen et al.,
768 2007). This mildly alkaline basalt has a slightly spikey "lithospheric" trace element pattern and
769 higher $^{87}Sr/^{86}Sr_i$ and lower εNd (Figure 12). It erupted shortly after the Spor Mountain rhyolite.
770 These two basalts represent the range of mafic magmas formed at the onset of Basin and Range
771 rifting. The isotopic composition of the Spor Mountain rhyolite is similar to that of the Mosida
772 Basalt (Fig. 12) suggesting melting of its intrusive equivalents could have generated the rhyolite.
773 Partial melting (~20%) of a Mosida Basalt composition followed by fractional crystallization
774 produces suitable Rb-Sr characteristics (purple line in Fig. 17A), but fails to produce the
775 compositions or trends for other elements including Be and Nb, which have much higher
776 concentrations in the model melts than observed (Fig. 17C-D). The isotopic compositions of the
777 Nye Canyon basalts with their high εNd values also precludes derivation of the Spor Mountain
778 rhyolite from intrusive underpinnings similar to them (Fig. 12)
779 Others have suggested that the highly-evolved rhyolites involve partial melting of
780 continental crust. Indeed, partial melting of the *upper continental crust* of Rudnick and Gao
781 (2014) followed by differentiation yields reasonable fits to the trace element data (orange line in
782 Fig. 17). The successful models involve ~20% partial melting, followed by extensive fractional
783 crystallization (f = 0.2 to 0.3). This two-stage scenario raises Be concentrations (2 ppm in the
784 source) to high levels (40 to 75 ppm) in the final residual liquid without resorting to extremely
785 small degrees of partial melting or extreme fractionation. However, the isotopic compositions

786 argue against the upper continental crust as a major source for the rhyolite. The age of the
787 continental basement in the eastern Great Basin is 2.0-2.6 Ga (Yonkee and Weil, 2015). The εNd
788 of 2.2 Ga crust with an upper crustal composition (Rudnick and Gao, 2014) would have been
789 about -25 in the Miocene and the $^{87}Sr/^{86}Sr$ ratio would have been about 0.726. Both of these are
790 far from the composition of the Spor Mountain rhyolite or Sheeprock Granite (about -7 and
791 0.706, respectively; Fig. 12).
792 In similar fashion, partial melting of Be-rich (~10 ppm) two-mica granite (Bikun, 1980),
793 which could be an important components of the crust in the northern Basin and Range province
794 (Farmer and DePaolo, 1983; Barnes et al., 2001; Lee et al., 2003), yields trace element
795 compositions similar to topaz rhyolites, if melting proceeds to about 50% before melt separation
796 and subsequent fractionation (blue lines in Fig. 17). Nonetheless, the Nd and Sr isotopic data
797 (Fig. 12) clearly show that the Be-rich Spor Mountain magma was not generated by partial
798 melting of Be-rich Mesozoic two-mica granite (or their metasedimentary protoliths). εNd of the
799 peraluminous granites in the Great Basin is much lower than of the rhyolites (εNd -25 vs -7).
800 In light of the relatively high εNd values found in the silicic rocks, more *mafic lower*
801 *crust* is another possible source for topaz rhyolites as suggested by Christiansen et al. (1988) and
802 Jacob et al. (2015). The Nd and Sr isotopic compositions of the Spor Mountain rhyolite and
803 Sheeprock Granite plot near the average composition of the Proterozoic mafic crust of northern
804 Colorado, as defined by Farmer et al. (2005) using xenolith data (Fig. 12). Likewise, the topaz-
805 bearing Mt. Cumulus stock of northern Colorado plots near this composition; Jacob et al. (2015)
806 concluded that the highly evolved Mt. Cumulus magma was derived from this mafic crust by low
807 degrees of partial melting. However, the lower crust could be quite variable across the region;
808 Wendlandt et al. (1993) report that the Nd-Sr isotopic composition of the mafic lower crust of

809 the southern Colorado Plateau ranges widely but does not overlap with the composition of the
810 Spor Mountain rhyolite of western Utah (pink region on Figure 12). Moreover, it is unlikely that
811 the crust under the Colorado Plateau is similar to that below Spor Mountain. Yonkee and Weil
812 (2015) conclude that the Yavapai province of northern Colorado (t_{DM}~1.7-2.0 Ga) extends only
813 as far west as eastern Utah and that western Utah and eastern Nevada basement is part of the
814 older Mojave province (t_{DM} ~ 2.0-2.6 Ga). Thus, partial melting of the mafic Precambrian crust
815 like that beneath Colorado and the Colorado Plateau is not the likely origin of the Spor Mountain
816 rhyolite and other A-type silicic magmas of the eastern Basin and Range province. Moreover,
817 trace element models (red lines in Fig. 17) show that even small degrees of partial melting of
818 lower continental crust (from Rudnick and Gao, 2014) followed by fractional crystallization
819 produces residual melts that are unlike topaz rhyolites with low concentrations of Rb, Nb, and
820 Be.

821 The final models we consider involve mixed or hybridized sources in the crust. For
822 example, Christiansen et al. (2007) proposed that mixing of a large component of contemporary
823 mantle-derived basalt and a smaller proportion of Proterozoic continental crust could be a source
824 of the topaz rhyolites in western Utah. To test this hypothesis, we examined mixtures of young
825 basalt and felsic crust of the ~2.2 Ma Mojave Province. Figure 12 shows mixing curves between
826 two potential mantle sources and a potential crustal source. We have used the "asthenospheric"
827 Nye Canyon basalts of central Nevada (Farmer et al., 2005) and the "lithospheric" Mosida Basalt
828 of central Utah (Christiansen et al., 2007) to represent the range of compositions for the mantle
829 end member. Both are Late Cenozoic basalts that are Nb-rich (they lack large negative Nb
830 anomalies) and formed contemporaneously with extension and with the eruption of topaz
831 rhyolites in the Basin and Range province. The composition of the crustal source is the average

two-mica granite used above. Simple mixing lines pass near the Spor Mountain isotopic composition. However, all of the trace element models involving a significant fraction of either the Late Cenozoic basalts produce magmas with Nb concentrations that exceed those of the rhyolites and lower concentrations of Rb, just as melts of the basalt alone (Fig. 17). Thus, it is unlikely that the rhyolites are derived from crust intruded by contemporaneous Nb-rich basalt.

Our preferred model uses a different sort of hybridized crust as a source for the Spor Mountain rhyolite. In the 20 m.y. that preceded the eruption of the Spor Mountain rhyolite, the western US experienced a voluminous southward sweep of volcanism created as part of a slab-rollback ignimbrite flareup (Coney, 1978). Thousands of cubic kilometers of andesite-dacite-rhyolite erupted during this episode (e.g. Lindsey, 1979; Best et al., 2013; Best et al., 2016). To produce this much magma, Johnson (1991) and Christiansen and Best (2014) have estimated that the crust of the western United States was thickened by ten kilometers or more. This process probably reconstituted the crust as a mixture of older Proterozoic basement and younger mafic intrusions or as a series extensively contaminated middle Cenozoic plutons. The isotopic composition of the most "juvenile" mafic to intermediate composition volcanic rocks of this middle Cenozoic episode are appropriate as sources of the topaz rhyolites (Fig. 12). We use an average middle Cenozoic andesite (Best et al., 2009) as a proxy for the composition of the hybridized crust of the Great Basin. Successful genetic models (Fig. 17) involve ~25% partial melting of this crustal hybrid, followed by extensive fractional crystallization (f = 0.2 to 0.3). Magma generated from this Nb-depleted but Rb-rich source produces partial melts with proportionately lower Nb and higher Rb than ones involving the contemporaneous Miocene basalts which were Nb-rich and Rb-poor. In addition to satisfying the isotopic constraints, this two-stage scenario raises Be concentrations, assumed to be 2 ppm in the hybrid source, to high

855 levels (40 to 75 ppm) in the final residual liquid without resorting to very small degrees of partial
856 melting or extreme fractionation.

857 **Petrogenetic summary.** In summary, we found convincing elemental and isotopic
858 evidence against several of the proposed mechanisms for the generation of Be-rich rhyolites in
859 the Great Basin of the western United States. Fractionation of mantle-derived basalt, partial
860 melting of the upper crust or of two-mica granites fail on isotopic grounds (Fig. 12). Partial
861 melting of lower crust or of crust extensively hybridized with contemporaneous mafic intrusions
862 do not satisfy trace element constraints (Fig. 17). Accordingly, we propose that when Miocene
863 Basin and Range extension started, hot basaltic magma was generated and then intruded in crust
864 previously hybridized by subduction zone magmas with relatively high Rb/Nb ratios. Heat
865 released from these intrusions produced rhyolitic partial melts that in some cases experienced
866 extensive fractional crystallization before eruption. This formed highly evolved rhyolite if the
867 degree of melting was relatively small ($f_{pm} \sim 0.25$) and fractionation was extensive ($f_{fc} \sim 0.2$ -
868 0.3). A three-step scenario (hybridization, partial melting, and fractional crystallization) explains
869 both the isotopic and elemental compositions of the Be-rich topaz rhyolite at Spor Mountain and
870 the evolved beryl-bearing granites of the Sheeprock Mountains.

871 **Implications**

872 The mineral/melt partitioning of elements one of the most basic processes that govern the
873 evolution of silicic magmas and is of special importance when applied to the generation of ore-
874 related rocks, such as the Be-mineralized Spor Mountain rhyolite. Often, the economic
875 concentration of an element in an ore body or its predecessor magma depends on the extent of
876 fractional crystallization and partition coefficients for that element. Further study of the
877 partitioning of rare elements (such as Be, Li, Sn, Mo, Nb, and Ta) and attendant intensive

878 parameters can lead to a better understanding of the mechanisms involved in concentrating them
879 into economically-viable ore deposits. Partition coefficients in the Be-mineralized Spor
880 Mountain rhyolite were similar to those in other high-silica rhyolites (e.g. Mahood and Hildreth,
881 1983; Nash and Crecraft, 1985; Bachmann et al., 2005). Important factors for Be concentration
882 were the enriched melt composition, low crystallization temperatures, and depolymerization of
883 the melt by the high F (and H_2O) content, as suggested by others (Manning, 1981; Webster et al.,
884 1987).

885 Furthermore, to constrain the pre-eruptive magmatic conditions, namely temperature,
886 pressure, water content, and viscosity, several methods were tested and compared to one another,
887 with general agreement. Melt temperatures were calculated using two feldspars, plagioclase-
888 liquid compositions, alkali feldspar saturation, Ti-in-quartz, and zircon saturation. Most of these
889 thermometers agreed within ± ~20 °C, which suggests that these thermometers, individually and
890 as a whole, give good results for low temperature, F-rich silicic magmas. However, Ti-in-Qz
891 thermometers yielded mixed estimates for pressure or temperature. The temperature and
892 viscosity of the F-rich, hydrous Spor Mountain melt were lower than for most other rhyolites and
893 these conditions may have assisted in the separation of crystals and liquids and promoted
894 extreme fractionation of the melts to elevated Be concentrations.

895 Our three-fold model for magma evolution involves prior inplating of the continental
896 crust with voluminous subduction-related mafic intrusions, partial melting (f_{pm} ~ 0.25) triggered
897 by subsequent injection of extension-related basalt, followed by fractional crystallization (f_{fc} ~
898 0.25). With the very low partition coefficients for Be measured here, this led to extreme
899 enrichments of Be and many other incompatible elements in the rhyolite. This set the stage for
900 later hydrothermal alteration, which further concentrated the Be into the underlying beryllium

tuff member, the host of the ore (Lindsey, 1977; Christiansen et al., 1984; Foley et al., 2012).

Acknowledgments

We are grateful for permission to sample and study materials from the Materion Brush Beryllium mine. The assistance of Emily Verplanck and G. Lang. Farmer in the isotope lab at the University of Colorado and David Tingey in the laboratories at Brigham Young University are appreciated. Reviews by Al Hofstra, an anonymous reviewer, and associate editor Celeste Mercer helped us clarify the presentation. This project was completed with instrumentation funding (for LA-ICP-MS, EMP, and XRF) from the U.S. National Science Foundation.

References

Adams, D.T., Hofstra, A., Cosca, M., Todorov, T., and Marsh, E. (2009) Age of sanidine composition of melt inclusions in quartz phenocrysts from volcanic rocks associated with large Mo and Be deposits in the western United States. GSA Annual Meeting.

Allegre, C.J., Treuil, M., Minster, J.F., Minster, B., and Albarede, F. (1977) Systematic use of trace element in igneous process; Part I, Fractional cyrstallization processes in volcanic suites. Contributions to Mineralogy and Petrology, 60(1), 57-75.

Anderson, A.T., Davis, A.M., and Lu, F. (2000) Evolution of Bishop Tuff rhyolitic magma based on melt and magnetite inclusions and zoned phenocrysts. Journal of Petrology, 41(3), 449-473.

Audetat, A. (2015) Compositional evolution and formation conditions of magmas and fluids related to porphyry Mo mineralization at Climax, Colorado. Journal of Petrology, 56(8), 1519-1546.

Audetat, A., and Li, W. (2017) The genesis of climax-type porphyry Mo deposits; insights from fluid inclusions and melt inclusions. Ore Geology Reviews, 88, 436-460.

Bachmann, O., Dungan, M.A., and Bussy, F. (2005) Insights into shallow magmatic processes in large silicic magma bodies; the trace element record in the Fish Canyon magma body, Colorado. Contributions to Mineralogy and Petrology, 149(3), 338-349.

Bacon, C.R., and Druitt, T.H. (1988) Compositional evolution of the zoned calcalkaline magma chamber of Mount Mazama, Crater Lake, Oregon. Contributions to Mineralogy and Petrology, 98(2), 224-256.

Barnes, C.G., Burton, B.R., Burling, T.C., Wright, J.E., and Karlsson, H.R. (2001) Petrology and geochemistry of the late Eocene Harrison Pass Pluton, Ruby Mountains core complex, northeastern Nevada. Journal of Petrology, 42(5), 901-930.

Bartels, A., Behrens, H., Holtz, F., Schmidt, B.C., Fechtelkord, M., Knipping, J., Crede, L., Baasner, A., and Pukallus, N. (2013) The effect of fluorine, boron and phosphorus on the viscosity of pegmatite forming melts. Chemical Geology, 346, 184-198.

Benisek, A., Dachs, E., and Kroll, H. (2010) A ternary feldspar-mixing model based on calorimetric data; development and application. Contributions to Mineralogy and Petrology, 160(3), 327-337.

Best, M.G., Barr, D.L., Christiansen, E.H., Gromme, S., Deino, A.L., and Tingey, D.G. (2009) The Great Basin Altiplano during the middle Cenozoic ignimbrite flareup; insights from volcanic rocks. International Geology Review, 51(7-8), 589-633.

Best, M.G., and Christiansen, E.H. (1991) Limited extension during peak Tertiary volcanism, Great Basin of Nevada and Utah. Journal of Geophysical Research, 96(B8), 13-13,528.

Best, M.G., Christiansen, E.H., de Silva, S.L., and Lipman, P.W. (2016) Slab-rollback ignimbrite flareups in the southern Great Basin and other Cenozoic American arcs; a distinct style of arc volcanism. Geosphere (Boulder, CO), 12(4), 1097-1135.

Best, M.G., Christiansen, E.H., Deino, A.L., Gromme, S., Hart, G.L., and Tingey, D.G. (2013) The 36-18 Ma Indian Peak-Caliente ignimbrite field and calderas, southeastern Great Basin, USA; multicyclic super-eruptions. Geosphere, 9(4), 864-950.

Bikun, J.V. (1980) Fluorine and lithophile element mineralization at Spor Mountain, Utah, Master's, p. 195. Arizona State University, Arizona State University, Tempe, AZ, United States (USA).

Boehnke, P., Watson, E.B., Trail, D., Harrison, T.M., and Schmitt, A.K. (2013) Zircon saturation re-revisited. Chemical Geology, 351, 324-334.

Boland, M.A. (2012) Beryllium; important for national defense. Fact Sheet - U. S. Geological Survey, 2.

Breiter, K., Svojtka, M., Ackerman, L., and Svecova, K. (2012) Trace element composition of quartz from the Variscan Altenberg-Teplice Caldera (Krusne hory/Erzgebirge Mts, Czech Republic/Germany); insights into the volcano-plutonic complex evolution. Chemical Geology, 326-327, 36-50.

Burt, D.M., and Sheridan, M.F. (1981) Model for the formation of uranium/lithophile element deposits in fluorine-rich volcanic rocks. AAPG Studies in Geology(13), 99-109.

Burt, D.M., Sheridan, M.F., Bikun, J.V., and Christiansen, E.H. (1982) Topaz rhyolites; distribution, origin, and significance for exploration. Economic Geology and the Bulletin of the Society of Economic Geologists, 77(8), 1818-1836.

Byrd, B.J., and Nash, W.P. (1993) Eruption of rhyolite at the Honeycomb Hills, Utah; cyclical tapping of a zoned silicic magma reservoir. Journal of Geophysical Research, 98(B8), 14-14,090.

Christiansen, E.H., Baxter, N., Ward, T.P., Zobell, E., Chandler, M.R., Dorais, M.J., Kowallis, B.J., and Clark, D.L. (2007) Cenozoic Soldiers Pass volcanic field, central Utah; implications for the transition to extension-related magmatism in the Basin and Range Province. Utah Geological Association Publication, 36, 123-142.

Christiansen, E.H., and Best, M.G. (2014) Constraints on the origin of subduction-related ignimbrite flareups from source volume calculations; the southern Great Basin ignimbrite province. Abstracts with Programs - Geological Society of America, 46(6), 374.

Christiansen, E.H., Bikun, J.V., Sheridan, M.F., and Burt, D.M. (1984) Geochemical evolution of topaz rhyolites from the Thomas Range and Spor Mountain, Utah. American Mineralogist, 69(3-4), 223-236.

Christiansen, E.H., Burt, D.M., Sheridan, M.F., and Wilson, R.T. (1983) The petrogenesis of topaz rhyolites from the Western United States. Contributions to Mineralogy and Petrology, 83(1-2), 16-30.

Christiansen, E.H., Keith, J.D., and Thompson, T.J. (1997) Origin of gem red beryl in Utah's Wah Wah Mountains. Mining Engineering, 49(2), 37-41.

Christiansen, E.H., Sheridan, M.F., and Burt, D.M. (1986) The Geology and Geochemistry of Cenozoic Topaz Rhyolites from the Western United States. Geological Society of America Special Papers, 205, 1-82.

Christiansen, E.H., Stuckless, J.S., Funkhouser-Marolf, M.J., and Howell, K.H. (1988) Petrogenesis of rare-metal granites from depleted crustal sources; an example from the Cenozoic of western Utah, U.S.A. Special Volume - Canadian Institute of Mining and Metallurgy, 39, 307-321.

Christiansen, E.H., and Venchiarutti, D.A. (1990) Magmatic inclusions in rhyolites of the Spor Mountain Formation, western Utah; limitations on compositional inferences from inclusions in granitic rocks. Journal of Geophysical Research, 95(B11), 17-17,728.

Coney, P.J. (1978) Mesozoic-Cenozoic Cordilleran plate tectonics. Memoir - Geological Society of America(152), 33-50.

Congdon, R.D., and Nash, W.P. (1991) Eruptive pegmatite magma; rhyolite of the Honeycomb Hills, Utah. American Mineralogist, 76(7-8), 1261-1278.

998 Dailey, S.R. (2016) Geochemistry of the Fluorine- and Beryllium-Rich Spor Mountain Rhyolite,
999 Western Utah. Department of Geological Sciences, Master of Science, p. 83. Brigham
1000 Young University.
1001 Eby, G.N. (1992) Chemical subdivision of the A-type granitoids; petrogenetic and tectonic
1002 implications. Geology (Boulder), 20(7), 641-644.
1003 Ekstroem, T.K. (1972) The Distribution of Fluorine among Some Coexisting Minerals.
1004 Contributions to Mineralogy and Petrology, 34(3), 192-200.
1005 Elkins, L.T., and Grove, T.L. (1990) Ternary feldspar experiments and thermodynamic models.
1006 American Mineralogist, 75(5-6), 544-559.
1007 Evensen, J.M., and London, D. (2002) Experimental silicate mineral/melt partition coefficients
1008 for beryllium and the crustal Be cycle from migmatite to pegmatite. Geochimica et
1009 Cosmochimica Acta (0016-7037), 66(12), 2239-2265.
1010 Evensen, J.M., London, D., and Wendlandt, R.F. (1999) Solubility and stability of beryl in
1011 granitic melts. American Mineralogist, 84(5-6), 733-745.
1012 Farmer, G.L., Bowring, S.A., Williams, M.L., Christensen, N.I., Matzel, J.P., and Stevens, L.
1013 (2005) Contrasting lower crustal evolution across an Archean-Proterozoic suture;
1014 physical, chemical and geochronologic studies of lower crustal xenoliths in southern
1015 Wyoming and northern Colorado. Geophysical Monograph, 154, 139-162.
1016 Farmer, G.L., Broxton, D.E., Warren, R.G., and Pickthorn, W. (1991) Nd, Sr, and O isotopic
1017 variations in metaluminous ash-flow tuffs and related volcanic rocks at the Timber
1018 Mountain/Oasis Valley Caldera Complex, SW Nevada; implications for the origin and
1019 evolution of large-volume silicic magma bodies. Contributions to Mineralogy and
1020 Petrology, 109(1), 53-68.
1021 Farmer, G.L., and DePaolo, D.J. (1983) Origin of Mesozoic and Tertiary granite in the western
1022 United States and implications for pre-Mesozoic crustal structure; 1, Nd and Sr isotopic
1023 studies in the geocline of the northern Great Basin. Journal of Geophysical Research,
1024 88(B4), 3379-3401.
1025 Farmer, G.L., Perry, F.V., Semken, S., Crowe, B., Curtis, D., and DePaolo, D.J. (1989) Isotopic
1026 evidence on the structure and origin of subcontinental lithospheric mantle in southern
1027 Nevada. Journal of Geophysical Research, 94(B6), 7885-7898.
1028 Foley, N.K., Hofstra, A.H., Lindsey, D.A., Seal, R.R., II, Jaskula, B., and Piatak, N.M. (2012)
1029 Occurrence model for volcanogenic beryllium deposits. Scientific Investigations Report,
1030 43.
1031 Frelinger, S.N., Ledvina, M.D., Kyle, J.R., and Zhao, D. (2015) Scanning electron microscopy
1032 cathodoluminescence of quartz; principles, techniques and applications in ore geology.
1033 Ore Geology Reviews, 65(PART 4), 840-852.
1034 Genson, A., Hanifi, A.R., Put, A.V., Pomeroy, M.J., and Hampshire, S. (2007) Effect of fluorine
1035 and nitrogen anions on properties of Ca-Si-Al-O glasses. Materials science forum, 554, p.
1036 31-35. Trans Tech Publ.
1037 Giordano, D., Russell, J.K., and Dingwell, D.B. (2008) Viscosity of magmatic liquids; a model.
1038 Earth and Planetary Science Letters, 271(1-4), 123-134.
1039 Hall, R.N. (1957) Variation of the distribution coefficient and solid solubility with temperature.
1040 Journal of Physics and Chemistry of Solids, 3(1), 63-73.
1041 Hanson, G.N. (1978) The application of trace elements to the petrogenesis of igneous rocks of
1042 granitic composition. Earth and Planetary Science Letters, 38(1), 26-43.

1043 Hildreth, W. (1979) The Bishop Tuff; evidence for the origin of compositional zonation in silicic
1044 magma chambers. Special Paper - Geological Society of America(180), 43-75.
1045 Hofstra, A.H., Todorov, T.I., Mercer, C.N., Adams, D.T., and Marsh, E.E. (2013) Silicate Melt
1046 Inclusion Evidence for Extreme Pre-eruptive Enrichment and Post-eruptive Depletion of
1047 Lithium in Silicic Volcanic Rocks of the Western United States: Implications for the
1048 Origin of Lithium-Rich Brines. Economic Geology, 108(7), 1691-1701.
1049 Huang, R., and Audétat, A. (2012) The titanium-in-quartz (TitaniQ) thermobarometer: a critical
1050 examination and re-calibration. Geochimica et Cosmochimica Acta, 84, 75-89.
1051 Humphreys, E.D. (1995) Post-Laramide removal of the Farallon Slab, Western United States.
1052 Geology (Boulder), 23(11), 987-990.
1053 Irber, W. (1999) The lanthanide tetrad effect and its correlation with K/Rb, Eu/Eu* , Sr/Eu,
1054 Y/Ho, and Zr/Hf of evolving peraluminous granite suites. Geochimica et Cosmochimica
1055 Acta, 63(3-4), 489-508.
1056 Jacob, K.H., Farmer, G.L., Buchwaldt, R., and Bowring, S.A. (2015) Deep crustal anatexis,
1057 magma mixing, and the generation of epizonal plutons in the southern Rocky Mountains,
1058 Colorado. Contributions to Mineralogy and Petrology, 169(1), Article 7.
1059 Johnson, C.M. (1991) Large-scale crust formation and lithosphere modification beneath middle
1060 to late Cenozoic calderas and volcanic fields, western North America. Journal of
1061 Geophysical Research, 96(B8), 13-13,507.
1062 Keppler, H. (1993) Influence of fluorine on the enrichment of high field strength trace elements
1063 in granitic rocks. Contributions to Mineralogy and Petrology, 114(4), 479-488.
1064 Kovalenko, V.I., Antipin, V.S., and Petrov, L.L. (1977) Distribution coefficients of beryllium in
1065 ongonites and some notes on its behavior in the rare metal lithium-fluorine-granites.
1066 Geochemistry International, 14(4), 129-141.
1067 Kularatne, K., and Audétat, A. (2014) Rutile solubility in hydrous rhyolite melts at 750–900° C
1068 and 2kbar, with application to titanium-in-quartz (TitaniQ) thermobarometry.
1069 Geochimica et Cosmochimica Acta, 125, 196-209.
1070 Lee, S.-Y., Barnes, C.G., Snoke, A.W., Howard, K.A., and Frost, C.D. (2003) Petrogenesis of
1071 Mesozoic, peraluminous granites in the Lamoille Canyon area, Ruby Mountains, Nevada,
1072 USA. Journal of Petrology, 44(4), 713-732.
1073 Lindsey, D.A. (1977) Epithermal beryllium deposits in water-laid tuff, western Utah. Economic
1074 Geology and the Bulletin of the Society of Economic Geologists, 72(2), 219-232.
1075 -. (1979) Geologic map and cross sections of Tertiary rocks in the Thomas Range and northern
1076 Drum Mountains, Juab County, Utah, p. 1 sheet. U. S. Geological Survey, Reston, VA.
1077 -. (1982) Tertiary volcanic rocks and uranium in the Thomas Range and northern Drum
1078 Mountains, Juab County, Utah. U. S. Geological Survey Professional Paper, 71.
1079 Lindsey, D.A., Shawe, D.R., and Erickson, R.L. (1982) Spor Mountain Be-F-U deposits. Open-
1080 File Report - U. S. Geological Survey, 67-69.
1081 Liu, Y., Anderson, A.T., Wilson, C.J.N., Davis, A.M., and Steele, I.M. (2006) Mixing and
1082 differentiation in the Oruanui rhyolitic magma, Taupo, New Zealand; evidence from
1083 volatiles and trace elements in melt inclusions. Contributions to Mineralogy and
1084 Petrology, 151(1), 71-87.
1085 Ludwig, K.R., Lindsey, D.A., Zielinski, R.A., and Simmons, K.R. (1980) U-Pb ages of
1086 uraniferous opals and implications for the history of beryllium, fluorine, and uranium
1087 mineralization at Spor Mountain, Utah. Earth and Planetary Science Letters, 46(2), 221-
1088 232.

Macdonald, R., Smith, R.L., and Thomas, J.E. (1992) Chemistry of the subalkalic silicic obsidians. U. S. Geological Survey Professional Paper, 214.

Mahood, G., and Hildreth, W. (1983) Large partition coefficients for trace elements in high-silica rhyolites. Geochimica et Cosmochimica Acta, 47(1), 11-30.

Manning, D.A.C. (1981) The effect of fluorine on liquidus phase relationships in the system Qz-Ab-Or with excess water at 1 kb. Contributions to Mineralogy and Petrology, 76(2), 206-215.

Marsh, B.D. (1981) On the crystallinity, probability of occurrence, and rheology of lava and magma. Contributions to Mineralogy and Petrology, 78(1), 85-98.

McCurry, M., Christiansen, E.H., and Leeman, W.P. (2008) Petrogenesis and volcanology of anorogenic rhyolites; a special issue dedicated to Bill Bonnichsen. Bulletin of Volcanology, 70(3), 247-434.

Mercer, C.N., Hofstra, A.H., Todorov, T.I., Roberge, J., Burgisser, A., Adams, D.T., and Cosca, M. (2015) Pre-Eruptive Conditions of the Hideaway Park Topaz Rhyolite: Insights into Metal Source and Evolution of Magma Parental to the Henderson Porphyry Molybdenum Deposit, Colorado. Journal of Petrology, 56(4), 645-679.

Moore, W.J., and Sorensen, M.L. (1978) Metamorphic rocks of the Granite Peak area, Tooele County, Utah. Abstracts with Programs - Geological Society of America, 10(5), 234.

Morgan, G.B.V.I., and London, D. (2005) Effect of current density on the electron microprobe analysis of alkali aluminosilicate glasses. American Mineralogist, 90(7), 1131-1138.

Munoz, J.L. (1984) F-OH and Cl-OH exchange in micas with applications to hydrothermal ore deposits. Reviews in Mineralogy, 13, 469-493.

Nash, W.P., and Crecraft, H.R. (1985) Partition coefficients for trace elements in silicic magmas. Geochimica et Cosmochimica Acta, 49(11), 2309-2322.

Neumann, H., Mead, J., and Vitaliand, C.J. (1954) Trace element variation during fractional crystallization as calculated from the distribution law. Geochimica et Cosmochimica Acta, 6(2-3), 90-99.

Onuma, N., Higuchi, H., Wakita, H., and Nagasawa, H. (1968) Trace element partition between two pyroxenes and the host lava. Earth and Planetary Science Letters, 5(1), 47-51.

Paton, C., Hellstrom, J., Paul, B., Woodhead, J., and Hergt, J. (2011) Iolite: Freeware for the visualisation and processing of mass spectrometric data. Journal of Analytical Atomic Spectrometry, 26(12), 2508-2518.

Pearce, J.A., Harris, N.B.W., and Tindle, A.G. (1984) Trace element discrimination diagrams for the tectonic interpretation of granitic rocks. Journal of Petrology, 25(4), 956-983.

Putirka, K.D. (2008) Thermometers and barometers for volcanic systems. Reviews in Mineralogy and Geochemistry, 69(1), 61-120.

Ramo, O.T., and Haapala, I. (1995) One hundred years of rapakivi granite. Mineralogy and Petrology, 52(3-4), 129-185.

Righter, K., and Carmichael, I.S.E. (1996) Phase equilibria of phlogopite lamprophyres from western Mexico; biotite-liquid equilibria and P-T estimates for biotite-bearing igneous rocks. Contributions to Mineralogy and Petrology, 123(1), 1-21.

Rogers, J.R. (1990) Origin of beryl in the Miocene Sheeprock Granite, west-central Utah, Master's, p. 69. Brigham Young University, Brigham Young University, Provo, UT, United States (USA).

Rudnick, R.L., and Gao, S. (2014) 4.1 - Composition of the Continental Crust A2 - Holland, Heinrich D. In K.K. Turekian, Ed. Treatise on Geochemistry (Second Edition), p. 1-51. Elsevier, Oxford.

Rusk, B. (2012) Cathodoluminescent Textures and Trace Elements in Hydrothermal Quartz. In J. Götze, and R. Möckel, Eds. Quartz: Deposits, Mineralogy and Analytics, p. 307-329. Springer Berlin Heidelberg, Berlin, Heidelberg.

Rusk, B.G., Reed, M.H., Dilles, J.H., and Kent, A.J.R. (2006) Intensity of quartz cathodoluminescence and trace-element content in quartz from the porphyry copper deposit at Butte, Montana. American Mineralogist, 91(8-9), 1300-1312.

Ryan, J.G. (2002) Trace-element systematics of beryllium in terrestrial materials. Reviews in Mineralogy and Geochemistry, 50, 121-145.

Severinghaus, J., and Atwater, T. (1990) Cenozoic geometry and thermal state of the subducting slabs beneath western North America. Memoir - Geological Society of America, 176, 1-22.

Shaw, D.M. (1970) Trace element fractionation during anatexis. Geochimica et Cosmochimica Acta, 34(2), 237-243.

Thomas, J.B., Watson, E.B., Spear, F.S., Shemella, P.T., Nayak, S.K., and Lanzirotti, A. (2010) TitaniQ under pressure; the effect of pressure and temperature on the solubility of Ti in quartz. Contributions to Mineralogy and Petrology, 160(5), 743-759.

Thomas, J.B., Watson, E.B., Spear, F.S., and Wark, D.A. (2015) TitaniQ recrystallized; experimental confirmation of the original Ti-in-quartz calibrations. Contributions to Mineralogy and Petrology, 169(3), Abstract 27.

Thomason, J.S., Atwell, R.J., Barnett, D.S., Bell, J.P., Fitzsimmons, M.F., Karvonides, N.S., and Kelly, J.C. (2013) Strategic and Critical Materials 2013 Report on Stockpile Requirements. IDA Paper NS P-4901. Alexandria, VA: Institute for Defense Analyses.

Webster, J.D., Holloway, J.R., and Hervig, R.L. (1987) Phase equilibria of a Be, U and F-enriched vitrophyre from Spor Mountain, Utah. Geochimica et Cosmochimica Acta, 51(3), 389-402.

Webster, J.D., Holloway, J.R., and Hervig, R.L. (1989) Partitioning of lithophile trace elements between H (sub 2) O and H (sub 2) O + CO (sub 2) fluids and topaz rhyolite melt. Economic Geology and the Bulletin of the Society of Economic Geologists, 84(1), 116-134.

Wen, S., and Nekvasil, H. (1994) SOLVCALC; an interactive graphics program package for calculating the ternary feldspar solvus and for two-feldspar geothermometry. Computers & Geosciences, 20(6), 1025-1040.

Wendlandt, E., DePaolo, D.J., and Baldridge, W.S. (1993) Nd and Sr isotope chronostratigraphy of Colorado Plateau lithosphere; implications for magmatic and tectonic underplating of the continental crust. Earth and Planetary Science Letters, 116(1-4), 23-43.

Wood, S.A. (1992) Theoretical prediction of speciation and solubility of beryllium in hydrothermal solution to 300°C at saturated vapor pressure: Application to bertrandite/phenakite deposits. Ore Geology Reviews, 7(4), 249-278.

Yonkee, W.A., and Weil, A.B. (2015) Tectonic evolution of the Sevier and Laramide belts within the North American Cordillera orogenic system. Earth-Science Reviews, 150, 531-593.

This is a preprint, the final version is subject to change, of the American Mineralogist (MSA)
Cite as Authors (Year) Title. American Mineralogist, in press.
DOI: https://doi.org/10.2138/am-2018-6256

1178

Figure captions

Figure 1. Geologic map of Spor Mountain and the surrounding area in west central Utah. The Be mines are located in the Beryllium Tuff Member of the Spor Mountain Formation (labeled 1 through 7). Samples of the rhyolites of the Spor Mountain Formation were taken from the following mines: 2-Taurus (SM-14, -831, -86), 4-Roadside (SM-31), and 7-Blue Chalk (SM-35, -37). Modified from Lindsey (1979). Red line in inset map is approximate eastern boundary of Basin and Range extension. BR = Basin and Range province and CP = Colorado Plateau and northern Rocky Mountains.

Figure 2. Representative photomicrographs of the three groups of rocks studied. (A) and (B) SM-14 (more evolved vitrophyre); (C) and (D) SM-31 (less evolved vitrophyre); (E) and F) SM-37 (less evolved devitrified). (G) and (H) show fluorite within SM-37. Note the more evolved samples have more phenocrysts than the less evolved samples. Biotite in the devitrified sample (E and F) has altered to magnetite and ilmenite. Qz = quartz; Sa = sanidine; Pl = plagioclase; Bt = biotite; Fl =fluorite.

Figure 3. Cathodoluminescence (CL) images of quartz phenocrysts in more evolved rhyolite SM-831(A and C) and less evolved SM-31 (B and D). Quartz commonly displays oscillatory zoning in CL images. Yellow numbers and circles correlate to Ti concentrations (ppm) determined by LA-ICP-MS. Grain B displays evidence of rapid growth in the form of skeletal edges, followed by infilling between the dendrites and trapping of melt inclusions.

Figure 4. Variation diagrams for the Spor Mountain rhyolite. More evolved (ME) rhyolites are those most enriched in incompatible elements and less evolved (LE) are those with lower concentrations of incompatible elements. (A) Total alkali silica plot with whole rock (WR, closed symbols) and matrix glass (MG, open symbols). All samples plot well within the rhyolite field, similar to other topaz rhyolites. Purple symbols are for other Spor Mountain analyses from Christiansen et al. (1984) (B) SiO_2 vs Be. (C) F vs Be. (D) F vs Cl. The compositions of rhyolite obsidians from Macdonald et al. (1992) are shown for comparison. (E) and (F) Tectonic discrimination diagrams (Pearce et al., 1984). All samples (with the exception of two matrix glass analyses from the more evolved group) plot in the "within plate" fields. Moreover, in (F) they plot in the A1 subfield (rift, plume, hotspot: Eby, 1992), consistent with the Spor Mountain rhyolite's continental rift setting.

Figure 5. Normalized trace element diagrams for the Spor Mountain rhyolite, Utah. (A) Rare earth element patterns for whole-rock (WR; solid lines) and matrix glass (MG; dashed lines). The more evolved rhyolites (ME) have lower REE as a result of the fractionation of REE accessory phases such as euxenite, fergusonite, and monazite compared to less evolved (LE) rhyolites. The devitrified (Dev) sample is similar to the less evolved rhyolite. The flat pattern for the HREE is common among topaz rhyolites (Christiansen et al., 1986).
(B) Primitive mantle normalized trace element patterns. The rhyolite lacks a negative Nb anomaly and has only a small positive Pb anomaly, consistent with its anorogenic origin. Barium and Sr anomalies suggest sanidine and sanidine fractionation; Ti anomaly suggests biotite separation, and P anomaly indicates apatite or xenotime fractionation.

Figure 6. Compositions of feldspars from the Spor Mountain rhyolite. Plotted for reference are feldspars from the Bishop Tuff (Hildreth, 1979) and topaz rhyolite lava from the Honeycomb Hills, Utah (Congdon and Nash, 1991). The solvus plotted is calculated at 700 °C and 2 kbar and 650 °C and 2 kbar, using SolvCalc (Wen and Nekvasil, 1994). (A) more evolved rhyolite, (B) less evolved rhyolite, and (C) devitrified less evolved rhyolite and comparison data.

Figure 7. Biotite in the Spor Mountain rhyolite is very Fe-rich. Red and blue symbols are fresh biotite in vitrophyres. Filled yellow circles are altered phenocrysts (AP), and open yellow circles are groundmass biotite (GB) in devitrified rocks. Plotted for reference are biotite compositions from the Bishop Tuff (Hildreth, 1979) and topaz rhyolite lava flows from the Honeycomb Hills, Utah (Congdon and Nash, 1991).

Figure 8. Mineral/melt partition coefficients for sanidine, plagioclase, and biotite in the Spor Mountain rhyolite. Elements are ordered based on compatibility in sanidine until Ba, and based on atomic number thereafter. Beryllium is highly incompatible in each mineral, Rb is compatible in biotite and incompatible in the feldspars, and Sr and Ba are among the most compatible elements in the system.

Figure 9. Partition coefficients for minerals in the Spor Mountain rhyolite compared to other silicic magmas (Mahood and Hildreth, 1983; Nash and Crecraft, 1985). Feldspars from the Spor Mountain rhyolite have partition coefficients similar to those in other silicic systems. Biotite from the Spor Mountain rhyolite has lower partition coefficients. The higher partition

coefficients for biotite in the Twin Peaks rhyolite lavas and the Bishop Tuff may be caused by inclusions of other minerals since these were calculated using analyses of mineral separates rather than laser spot analyses.

Figure 10. Onuma et al. (1968) diagram with mineral/melt partition coefficients for sanidine, plagioclase, and biotite, using averages for each mineral. Curves for different ionic charges are in color. Solid lines are well constrained by measurements whereas dotted lines are best estimates. The estimated size of each site is given in angstroms.

Figure 11. Comparison of partition coefficients for Be between melt and sanidine, plagioclase, biotite, and quartz. Data from Kovalenko et al. (1977), Evensen et al. (1999), Evensen and London (2002), and this paper.

Figure 12. εNd_t vs $^{87}Sr/^{86}Sr_t$ for the Spor Mountain rhyolite and Sheeprock Granite. The late Cenozoic extension-related Nye Canyon basalts (Farmer et al., 2005) and Mosida Basalt (Christiansen et al., 2007) represent two possible mantle components present in Great Basin magmas. The average composition of crustal xenoliths from the Colorado Plateau (Wendlandt et al., 1993; Jacob et al., 2015), middle Cenozoic andesite from the Great Basin (Best et al., 2009), and an average two-mica granite from the region represent three possible crustal sources. Possible crustal hybrids between crust and mantle are shown as simple mixing lines; purple crosses are at 10% increments.

Figure 13. Phase diagram for the Spor Mountain rhyolite at 2 kbar, modified from Webster et al. (1987). The Spor Mountain rhyolite crystallized at about 700 °C at 2 kbar and under water-undersaturated conditions. Qz = quartz; Sa = sanidine; Pl = plagioclase; Bt = biotite.

Figure 14. Pressure-dependent temperatures calculated for (A) SM-31, a less evolved rhyolite and (B) SM-831, a more evolved rhyolite. The degree of pressure sensitivity can be estimated by the slopes of the curves. The intersections of these thermobarometric curves are estimates of the crystallization pressure of the system. The Huang and Audétat (2012) Ti in Qz curve crosses most of the less pressure sensitive thermobarometers between 1-3 kbar, while the Thomas et al. (2010) model for Ti-in-quartz requires a crystallization pressure of 5 to 13 kbar, much too high for this volcanic system as indicated by the phase equilibrium study of Webster et al. (1987).

Figure 15. Trends for partial melting (PM, dashed lines), vs. fractional crystallization (FC, solid lines) involving compatible elements (A) Zr and (B) Y. The ratio of Be°/Be serves as an estimate of f —the fraction of liquid in the system. Bulk partition coefficients (D) from this study are given. Based on these models, variable degrees of partial melting cannot account for the strong depletions of the compatible trace elements in the more evolved Spor Mountain magma but fractional crystallization can.

Figure 16. Be variation diagrams for the Spor Mountain rhyolite. (A) Be vs. Ta (an incompatible element) and (B) Be vs. Y (a compatible element) for whole rocks and glass matrix. Blue lines and solid symbols are for whole-rocks (WR) and green lines and open symbols are for matrix

glass (MG). The bulk partition coefficient *D* is derived from the slope of the line using the method of Allegre et al. (1977).

Figure 17. Trace element models depicting the origin and evolution of the Spor Mountain rhyolite, assuming five different protoliths. Parameters for the models are given in Table 7. The model curves are compared to the rock compositions (dots) on two-element variation diagrams (A) Rb-Sr, (B) Nb-Sr, (C) Rb-Be, and (D) Rb-Nb. Two calculated liquid lines of descent are given for each protolith (see text)—one for batch partial melting (bold line) and another for fractional crystallization (fine line). Crosses are at 10% melt increments. It is possible to get Spor Mountain compositions by extensive fractional crystallization of a 20-25% partial melt of upper continental crust (orange) or of crust hybridized by middle Cenozoic intrusions (represented by average andesite from the Great Basin; cyan lines). Data sources: Mosida Basalt (Christiansen et al., 2007), two-mica granite (Barnes et al., 2001), Great Basin andesite (Best et al., 2009), lower continental crust (Farmer et al., 2005; Jacob et al., 2015), and upper continental crust (Rudnick and Gao, 2014).

Supplementary Figure 1. Forward modeling of fractional crystallization in the Spor Mountain rhyolite. Data points in red represent the less evolved rhyolites (SM-31 and -35), and are assumed to be the parental liquid (i.e. $f = 1$; 100% melt); blue symbols represent the more evolved magma (SM-831 and -86). Lines represent the liquid lines of descent, with purple crosses at 10% melt increments. Numbers next to line indicate melt fraction (*f*). The compositions of the more evolved rhyolites plot between 55% and 60% residual melt fraction.

This is a preprint, the final version is subject to change, of the American Mineralogist (MSA)
Cite as Authors (Year) Title. American Mineralogist, in press.
DOI: https://doi.org/10.2138/am-2018-6256

Supplementary Figure 2. Cathodoluminesence images of quartz phenocrysts in the Spor Mountain rhyolite. Sample numbers are given.

This is a preprint, the final version is subject to change, of the American Mineralogist (MSA)
Cite as Authors (Year) Title. American Mineralogist, in press.
DOI: https://doi.org/10.2138/am-2018-6256

Table 1. Composition of Spor Mountain rhyolite

Sample	SM-31	SM-35	SM-37	SM-14	SM-831[d]	SM-831[e]	SM-86
Lithology[a]	V	V	D	V	V	V	V
Group[b]	LE	LE	LE	ME	ME	ME	ME
Main oxides (wt. %)							
SiO_2	75.02	75.44	75.48	74.03	74.49	73.90	74.16
TiO_2	0.05	0.03	0.05	0.02	0.03	0.00	0.03
Al_2O_3	13.52	13.48	13.38	14.44	14.31	14.84	14.38
Fe_2O_3	1.42	1.45	1.41	1.07	1.04	0.89	1.09
MnO	0.06	0.05	0.03	0.06	0.06	0.06	0.06
MgO	0.04	0.07	0.04	0.03	0.03	0.02	0.01
CaO	0.51	1.05	0.44	0.42	0.34	0.26	0.39
Na_2O	4.12	4.60	4.11	4.65	4.55	4.69	4.68
K_2O	5.24	3.80	5.05	5.26	5.13	5.33	5.19
P_2O_5	0.01	0.01	0.01	0.01	0.01	0.01	0.01
LOI[c]	3.30	3.79	0.48	2.96	3.01	n.m.	3.23
Anal Total	99.47	99.56	98.98	99.05	99.06	99.83	99.16
Trace elements (ppm)							
As	18	14	5.0	35	29	n.m.	36
Ba	20	21	30	20	19	n.m.	20
Be	39	36	13	64	58	n.m.	58
Ce	141	136	141	118	117	107	118
Cr	4.8	4.6	10	5.5	5.6	1.5	5.4
Cs	55	59	23	87	81	n.m.	85
Cu	1.4	2.8	1.6	1.8	0.8	4.0	0.9
Dy	17	18	16	11	11	n.m.	11
Er	12	12	11	7.5	7.7	n.m.	7
Ga	39	32	34	37	38	39	38
Gd	15	15	14	9	9	n.m.	10
Hf	7.0	6.9	7.0	6.8	6.6	n.m.	6.3
Ho	3.5	3.5	3.2	2.3	2.3	n.m.	2.2
La	61	58	55	51	50	48	54
Li	50	70	190	90	130	n.m.	110
Lu	1.9	1.9	1.8	1.7	1.6	n.m.	1.4
Mo	2.0	1.0	1.0	1.0	1.0	n.m.	1.0
Nb	122	133	143	134	136	147	130
Nd	60	59	59	48	50	38	52
Ni	1.4	1.3	1.4	2.0	1.0	1.0	0.6
Pb	51	49	45	45	49	49	44
Pr	18	17	15	15	15	n.m.	14
Rb	925	1001	881	1317	1273	1540	1285
Sc	2.4	2.7	1.7	1.8	2.0	n.m.	1.7
Sm	14	15	13	11	11	8.6	11
Sn	33	32	15	45	42	n.m.	42
Sr	4	5	6	2	3	n.m.	2
Ta	25	25	25	37	36	n.m.	35
Tb	2.6	2.7	2.4	1.8	1.7	n.m.	1.8
Th	66	67	69	47	47	42	47
Tl	10	10	10	10	10	n.m.	10
Tm	1.8	1.8	1.7	1.4	1.4	n.m.	1.2
U	34	35	13	30	31	38	27
V	5.0	2.7	3.4	2.7	5.0	1.4	2.7
Y	112	128	112	80	80	48	73
Yb	13	13	12	11	11	n.m.	10
Zn	96	92	39	49	49	51	50
Zr	127	132	138	102	101	107	99

Notes: Normalized to 100% on a volatile-free basis.

[a] V = vitrophyre; D = devitrified

[b] LE = Less evolved; ME = More evolved

[c] LOI = loss on ignition at 1000ºC for four hours.

[d] Analyses are for whole-rock data.

[e] Analyses are for matrix glass separate.

n.m. = not measured.

This is a preprint, the final version is subject to change, of the American Mineralogist (MSA)
Cite as Authors (Year) Title. American Mineralogist, in press.
DOI: https://doi.org/10.2138/am-2018-6256

Table 2. Composition of Spor Mountain rhyolite matrix glass

Sample	SM-31	SM-35	SM-14	SM-831	SM-86
Lithology[a]	V	V	V	V	V
Group[b]	LE	LE	ME	ME	ME
	N = 25	N = 9	N = 18	N = 22	N = 20
			Main oxides (wt. %)		
SiO_2	77.30	77.79	76.70	75.82	76.02
TiO_2	0.03	0.03	0.01	0.01	0.02
Al_2O_3	13.45	14.11	14.50	14.60	14.30
FeO_t	1.14	1.26	0.39	0.40	0.62
MnO	0.07	0.05	0.09	0.07	0.06
MgO	0.00	0.01	0.01	0.00	0.00
CaO	0.32	0.18	0.03	0.03	0.17
Na_2O	3.02	3.06	3.60	3.98	4.21
K_2O	4.66	3.49	4.68	5.09	4.60
P_2O_5	0.00	0.02	0.00	0.00	0.00
F	0.89	0.46	1.58	1.45	1.65
Cl	0.31	0.27	0.17	0.20	0.20
Anal total	96.80	94.43	97.32	97.14	96.82

	Trace elements (ppm)														
	Average N = 15	SD	Rel. SD (%)	Average N = 17	SD	Rel. SD (%)	Average N = 3	SD	Rel. SD (%)	Average N = 18	SD	Rel. SD (%)	Average N = 12	SD	Rel. SD (%)
Li	72	34.5	48	75	27.9	37	154	8.1	5	99	62.6	63	106	64.9	61
Be	40	10.7	26	43	10.6	25	66	54.8	83	75	7.7	10	74	36.4	49
B	119	32.6	27	106	54.1	51	30	4.9	16	216	45.2	21	163	20.0	12
Zn	87	44.3	51	94	37.2	39	44	22.9	52	52	8.8	17	47	13.7	29
Ga	29	7.5	26	29	1.4	5	36	5.5	15	38	2.4	6	33	1.5	5
Rb	1049	272.2	26	1278	602.6	47	1745	249.4	14	1782	79.8	4	1645	847.3	51
Sr	1	0.4	47	2	1.0	59	5	0.1	3	0.3	0.1	58	1	0.9	100
Y	69	2.9	4	81	7.9	10	60	38.0	63	16	4.0	26	13	5.2	39
Zr	66	23.6	36	76	7.2	10	n.d.	-	-	38	4.6	12	33	9.7	29
Nb	116	30.0	26	114	37.7	33	420	311.8	74	138	4.4	3	136	39.3	29
Mo	2	1.0	49	2	0.7	38	2	0.3	16	2	0.9	42	2	0.6	36
Sn	33	13.8	42	32	10.9	34	13	3.3	26	47	22.1	47	47	21.4	46
Cs	65	17.2	26	73	29.3	40	19	4.1	22	119	51.1	43	114	51.8	45
Ba	2	0.9	46	3	1.3	43	5	1.0	22	1	0.2	33	1	0.2	41
La	46	16.3	35	50	16.7	34	n.d.	-	-	26	6.6	25	26	7.7	29
Ce	143	50.5	35	141	2.4	2	n.d.	-	-	88	5.7	7	94	27.1	29
Pr	15	0.5	3	15	5.0	33	n.d.	-	-	8	3.2	39	9	2.5	29
Nd	50	1.7	3	52	4.9	9	n.d.	-	-	22	2.7	12	22	6.6	30
Sm	12	1.3	11	12	1.2	9	n.d.	-	-	4	1.8	40	4	0.5	11
Gd	9	2.3	27	11	1.1	11	7	2.1	30	3	1.3	43	3	0.8	32
Tb	2	0.6	36	2	0.2	10	1	0.6	43	1	0.2	41	0.5	0.2	46
Dy	10	3.4	36	12	1.1	9	9	5.3	61	4	1.0	29	3	1.0	30
Ho	2	0.6	27	2	0.2	9	2	1.1	60	1	0.2	28	1	0.2	31
Er	6	1.7	26	7	1.9	26	5	2.9	58	2	0.9	39	2	0.7	32
Yb	8	3.0	35	10	0.9	9	8	6.2	81	5	1.8	34	4	1.3	32
Lu	1	0.1	11	1	0.4	26	1	0.8	75	1	0.3	40	1	0.1	12
Hf	4	1.5	37	5	0.7	15	7	10.6	158	4	1.6	43	3	0.9	30
Ta	29	13.3	46	30	7.4	24	16	1.2	7	50	12.4	25	51	14.7	29
W	23	6.1	26	24	7.8	33	14	2.1	15	40	9.7	24	39	11.2	29
Pb	47	19.6	41	48	11.8	24	54	5.9	11	40	9.7	24	36	1.1	3
Th	42	1.9	5	47	3.6	8	51	16.7	33	22	2.4	11	21	6.2	29
U	33	14.9	46	34	0.8	2	n.d.	-	-	25	8.1	32	25	7.2	29

Notes: Major elements normalized to 100% on a volatile-free basis. Compositions are averages of each sample.

[a] V = vitrophyre; D = devitrified

[b] LE = Less evolved; ME = More evolved

SD = 1σ standard deviation

Rel. SD = relative standard deviation (average divided by standard deviation)

n.d. = not detected

This is a preprint, the final version is subject to change, of the American Mineralogist (MSA)
Cite as Authors (Year) Title. American Mineralogist, in press.
DOI: https://doi.org/10.2138/am-2018-6256

Table 3. Eruption temperature (°C) estimates for the Spor Mountain rhyolite at 2 kbar and 5 wt% $_2$O

Sample		SM-31		SM-35		SM-37		SM-14		SM-831		SM-86	
Lithology[a]	Thermometer	V		V		D		V		V		V	
Group[b]	Model	LE		LE		LE		ME		ME		ME	
		Average	SD	Average	SD	Average	SD	Average	SD	Average	SD	Average	SD
Boehnke et al., 2013[c]	Zrn-sa. (MG)	689	34	724	9	n.c.	-	n.c.	-	633	10	619	23
Boehnke et al., 2013[d]	Zrn-sat. (WR)	715	10	716	11	726	12	692	11	696	15	690	17
Putirka, 2008[e]	Pl-Liq	763	3	754	3	n.c.	-	701	5	703	5	752	5
Putirka, 2008[f]	Afs-Liq	752	2	693	2	n.c.	-	693	3	678	4	698	1
Putirka, 2008[g]	Two Fsp	704	3	711	3	n.c.	-	682	11	668	7	663	9
Elkins & Grove, 1990[h]	Two Fsp	707	4	715	4	739	5	648	25	670	13	665	20
Benisek, 2010[i]	Two Fsp	709	13	724	13	732	15	629	35	653	28	641	36
Huang and Audetat, 2012[j]	Ti-in-Qz	678	18	689	19	n.c.	-	n.c.	-	703	14	702	28
Thomas et al., 2010[k]	Ti-in-Qz	536	14	545	15	n.c.	-	n.c.	-	556	11	555	22
Righter et al., 1996[l]	Biotite	799	3	804	3	n.c.	-	783	5	787	6	788	7
a TiO_2[m]		0.39	0.10	0.35	0.10	n.c.	-	n.c.	-	0.18	0.10	0.24	0.20

Notes:

[a] V = vitrophyre; D = devitrified

[b] LE = Less evolved; ME = More evolved

[c] Zr saturation temperature from Boehnke et al. (2013), using matrix glass (MG) compositions.

[d] Zr saturation temperature from Boehnke et al. (2013), using whole-rock (WR) compositions.

[e] Plagioclase-liquid temperature from Putirka (2008), equation (24a).

[f] Alkali feldspar-liquid temperature from Putirka (2008), equation (24b).

[g] Two feldspar temperature from Putirka (2008), equation (27b).

[h] Two feldspar temperature from Elkins and Grove (1990).

[i] Two feldspar temperature from Benisek et al. (2010).

[j] Ti-in-quartz temperature from Huang and Audetat (2012).

[k] Ti-in-quartz temperature from Thomas et al. (2010).

[l] Biotite temperature from Righter et al. (1996), using TiO_2 in matrix glass.

[m] Calculated using the method developed by Kularatne and Audetat (2014).

n.c. = not calculated

This is a preprint, the final version is subject to change, of the American Mineralogist (MSA)
Cite as Authors (Year) Title. American Mineralogist, in press.
DOI: https://doi.org/10.2138/am-2018-6256

Table 4. Partition coefficients for sanidine, plagioclase, biotite, and quartz in the Spor Mountain rhyolite

Sample	SM-31				SM-35				SM-831				SM-86			
Lithology[a]	V				V				V				V			
Group[b]	LE				LE				ME				ME			
	Sanidine	Plagioclase	Biotite	Quartz	Sanidine	Plagioclase	Biotite	Quartz	Sanidine	Plagioclase	Biotite	Quartz	Sanidine	Plagioclase	Biotite	Quartz
Li	0.15	0.54	4.81	0.64	0.15	0.28	4.72	0.67	0.14	0.26	9.95	0.27	0.19	0.22	9.55	0.47
Be	0.07	0.25	0.05	n.d.	0.05	0.18	0.04	n.d.	0.04	0.13	0.04	n.d.	0.05	0.12	0.04	n.d.
B	0.50	0.50	0.41	0.54	0.74	0.65	0.43	0.43	5.76	0.39	0.29	0.50	0.41	0.47	0.28	0.33
Al	n.d.	n.d.	n.d.	0.00	n.d.	n.d.	n.d.	0.00	n.d.	n.d.	n.d.	0.00	n.d.	n.d.	n.d.	0.00
P	n.d.	n.d.	n.d.	0.19	n.d.	n.d.	n.d.	0.18	n.d.	n.d.	n.d.	0.08	n.d.	n.d.	n.d.	0.10
Ti	n.d.	n.d.	n.d.	0.15	n.d.	n.d.	n.d.	0.14	n.d.	n.d.	n.d.	0.22	n.d.	n.d.	n.d.	0.19
Fe	n.d.	n.d.	n.d.	0.00	n.d.	n.d.	n.d.	0.00	n.d.	n.d.	n.d.	0.00	n.d.	n.d.	n.d.	0.00
Zn	0.28	0.18	13.80	n.d.	0.11	n.d.	13.50	n.d.	n.d.	0.10	22.70	n.d.	0.31	n.d.	20.90	n.d.
Ga	1.10	1.31	3.00	n.d.	1.04	1.25	3.18	n.d.	0.88	1.11	3.32	n.d.	0.98	1.23	3.49	n.d.
Rb	0.48	0.04	2.06	n.d.	0.40	0.16	2.29	n.d.	0.29	0.02	1.36	n.d.	0.42	0.02	2.19	n.d.
Sr	14.7	21.1	1.5	n.d.	7.19	7.8	1.0	n.d.	2.26	10.1	2.7	n.d.	7.78	4.5	2.5	n.d.
Y	0.00	0.03	0.09	n.d.	0.01	0.00	0.00	n.d.	n.d.	0.01	0.16	n.d.	0.03	0.02	0.14	n.d.
Zr	0.02	0.05	0.08	n.d.	0.02	n.d.	0.08	n.d.	n.d.	0.01	0.08	n.d.	0.03	0.03	0.12	n.d.
Nb	0.02	0.09	8.08	n.d.	0.03	n.d.	8.74	n.d.	0.00	0.00	7.96	n.d.	0.02	0.01	8.78	n.d.
Mo	n.d	n.d	1.09	n.d.	n.d	n.d	1.29	n.d.	n.d	n.d	1.14	n.d.	n.d	n.d	1.08	n.d.
Sn	0.14	0.15	0.36	n.d.	0.11	n.d.	0.40	n.d.	0.39	0.07	0.97	n.d.	0.07	0.07	1.05	n.d.
Cs	0.07	0.22	0.57	n.d.	0.07	n.d.	0.67	n.d.	0.15	0.13	0.28	n.d.	0.17	0.17	0.80	n.d.
Ba	13.2	1.3	14.6	n.d.	8.19	3.5	8.0	n.d.	4.84	0.7	36.4	n.d.	7.27	1.4	5.7	n.d.
La	0.15	0.26	0.38	n.d.	0.12	0.23	0.07	n.d.	n.d.	0.44	n.d.	n.d.	0.27	0.49	0.16	n.d.
Ce	0.06	0.14	0.32	n.d.	0.05	0.11	0.03	n.d.	n.d.	0.23	n.d.	n.d.	0.10	0.22	0.15	n.d.
Pr	0.02	0.09	0.30	n.d.	0.02	0.07	0.09	n.d.	n.d.	0.16	n.d.	n.d.	0.04	0.16	0.17	n.d.
Nd	0.02	0.07	0.30	n.d.	0.01	0.05	0.11	n.d.	n.d.	0.15	n.d.	n.d.	0.05	0.13	0.36	n.d.
Sm	n.d	n.d	0.30	n.d.	n.d	n.d	0.16	n.d.	n.d	n.d	n.d.	n.d.	n.d	n.d	0.77	n.d.
Gd	n.d	n.d	0.34	n.d.	n.d	n.d	0.14	n.d.	n.d	n.d	n.d.	n.d.	n.d	n.d	1.92	n.d.
Tb	n.d	n.d	0.29	n.d.	n.d	n.d	0.16	n.d.	n.d	n.d	n.d.	n.d.	n.d	n.d	1.38	n.d.
Dy	n.d	n.d	0.28	n.d.	n.d	n.d	0.18	n.d.	n.d	n.d	n.d.	n.d.	n.d	n.d	1.96	n.d.
Ho	n.d	n.d	0.27	n.d.	n.d	n.d	0.25	n.d.	n.d	n.d	n.d.	n.d.	n.d	n.d	1.96	n.d.
Er	n.d	n.d	0.29	n.d.	n.d	n.d	0.15	n.d.	n.d	n.d	n.d.	n.d.	n.d	n.d	2.52	n.d.
Yb	n.d	n.d	0.31	n.d.	n.d	n.d	0.12	n.d.	n.d	n.d	n.d.	n.d.	n.d	n.d	1.40	n.d.
Lu	n.d	n.d	0.29	n.d.	n.d	n.d	0.05	n.d.	n.d	n.d	n.d.	n.d.	n.d	n.d	0.23	n.d.
Hf	n.d	n.d	0.13	n.d.	n.d	n.d	0.06	n.d.	n.d	n.d	0.15	n.d.	n.d	n.d	0.14	n.d.
Ta	0.01	0.06	1.47	n.d.	0.01	n.d.	1.96	n.d.	0.02	0.00	1.01	n.d.	0.01	0.03	1.61	n.d.
W	n.d	n.d	0.05	n.d.	n.d	n.d	0.07	n.d.	n.d	n.d	0.04	n.d.	n.d	n.d	0.08	n.d.
Pb	1.20	0.68	0.18	n.d.	1.20	0.87	0.20	n.d.	1.08	1.11	0.19	n.d.	2.08	1.10	0.23	n.d.
Th	0.01	0.09	0.10	n.d.	0.01	n.d.	0.01	n.d.	n.d.	n.d.	n.d.	n.d.	0.07	n.d.	3.30	n.d.
U	0.01	0.04	0.10	n.d.	0.04	n.d.	0.02	n.d.	n.d.	n.d.	0.06	n.d.	0.01	0.03	0.03	n.d.

Notes:

[a] V = vitrophyre; D = devitrified

[b] LE = Less evolved; ME = More evolved

n.d. = not detected

This is a preprint, the final version is subject to change, of the American Mineralogist (MSA)
Cite as Authors (Year) Title. American Mineralogist, in press.
DOI: https://doi.org/10.2138/am-2018-6256

Table 5. Isotope data for Spor Mountain rhyolite and Sheeprock Granite

Sample	SM-31	SM-35	SR-108	SR-581	SR-1381
Lithology[a]	V	V			
Group[b]	LE	LE			
	Spor Mountain		Sheeprock Granite		
$^{87}Sr/^{86}Sr_i$[c]	n.m.	n.m.	0.7064	0.7064	0.7064
εNd_i[d]	-7.81	-7.18	-5.9	-6.3	-4.8
$^{206}Pb/^{204}Pb$	18.96	n.m.	n.m.	18.95	18.85
$^{207}Pb/^{204}Pb$	15.65	n.m.	n.m.	15.64	15.64
$^{208}Pb/^{204}Pb$	39.21	n.m.	n.m.	39.03	38.93

Notes:

[a] V = vitrophyre; D = devitrified

[b] LE = Less evolved; ME = More evolved

[c] Based on Rb-Sr isochron

[d] Corrected to 21 Ma.

n.m. = not measured

This is a preprint, the final version is subject to change, of the American Mineralogist (MSA)
Cite as Authors (Year) Title. American Mineralogist, in press.
DOI: https://doi.org/10.2138/am-2018-6256

Table 6. Bulk partition coefficients calcualted using the inverse modeling approach

	r^2	m	$\overline{D}$	C_L	C_O	f
Li	0.96	0.77	0.23	139	77	0.46
Be	1.00	1.00	0.00	74	42	0.57
B	0.89	0.95	0.05	190	113	0.58
Zn	0.95	-1.16	2.16	49	94	0.57
Ga	0.85	0.35	0.65	35	29	0.57
Rb	0.84	0.66	0.34	1729	1218	0.59
Sr	0.53	-1.74	2.74	0.6	2.5	0.44
Y	0.97	-2.91	3.91	14	75	0.57
Zr	0.94	-1.26	2.26	36	73	0.56
Nb	0.97	0.28	0.72	135	115	0.56
Sn	0.96	0.56	0.44	48	35	0.56
Cs	0.98	0.85	0.15	115	72	0.57
La	0.97	-1.08	2.08	26	49	0.57
Ce	1.00	-0.82	1.82	90	143	0.57
Pr	0.99	-1.06	2.06	8.3	15	0.57
Nd	0.99	-1.50	2.50	22	51	0.57
Sm	0.97	-1.80	2.80	4.3	12	0.57
Gd	0.96	-2.17	3.17	2.8	9.7	0.57
Dy	0.96	-2.05	3.05	3.4	11	0.57
Ho	0.96	-1.39	2.39	0.7	2.2	0.42
Er	0.95	-1.96	2.96	2.3	6.9	0.57
Yb	0.86	-1.23	2.23	4.6	9.2	0.57
Hf	0.80	-0.62	1.62	3.2	4.6	0.56
Ta	1.00	0.92	0.08	50	29	0.57
W	0.99	0.88	0.12	39	24	0.57
Pb	0.88	-0.40	1.40	38	48	0.56
Th	0.96	-1.26	2.26	22	45	0.56
U	0.96	-0.52	1.52	25	33	0.57

Notes:

r^2 = correlation value from trace element variation diagrams

m = slope of line on logarithmic variation diagrams (Figure 13)

$\overline{D} = 1 - m$

C_L = concentration of element i in differentiated melt (average of matrix glass from evolved samples)

C_O = concentration of element i in parental melt (average of matrix glass from less evolved samples)

f = fraction of residual liquid

This is a preprint, the final version is subject to change, of the American Mineralogist (MSA)
Cite as Authors (Year) Title. American Mineralogist, in press.
DOI: https://doi.org/10.2138/am-2018-6256

Table 7. Parameters used in trace element models depicted in Fig. 16

	F_{bpm}	Rb_o	D_{Rb}	Sr_o	D_{Sr}	Be_o	D_{Be}	Nb_o	D_{Nb}	Y_o	D_Y	Cr_o	D_{Cr}	Ni_o	D_{Ni}
Batch Partial Melting															
Upper Continental Crust[a]	0.20	84	0.05	320	3.5	2	0.03	12	0.10	21	0.6	92	3.2	47	2.6
Lower Continental Crust[b]	0.20	11	0.05	348	3.5	1	0.03	5	0.10	16	0.6	215	3.2	88	2.6
Average Great Basin Andesite[c]	0.25	109	0.05	685	3.5	2	0.03	14	0.10	29	0.6	69	3.2	17	2.6
Two-mica granite[d]	0.50	255	0.34	475	3.5	5	0.03	17	0.10	23	0.6	4	3.2	4	2.6
Mosida Basalt[e]	0.20	43	0.10	884	3.5	3	0.03	39	0.10	28	0.6	26	3.2	16	2.6
Fractional Crystallization															
Upper Continental Crust[a]		350	0.30	107	3.4	10	0.03	43	0.15	31	0.6	33	3.2	21	2.6
Lower Continental Crust[b]		46	0.30	116	3.0	7	0.03	18	0.10	24	0.6	78	3.2	39	2.6
Average Great Basin Andesite[c]		379	0.30	238	3.5	9	0.03	43	0.20	41	0.6	26	3.2	8	2.6
Two-mica granite[d]		381	0.30	211	3.5	10	0.03	31	0.20	29	0.6	2	3.2	2	2.6
Mosida Basalt[e]		152	0.20	295	3.0	14	0.03	139	0.10	41	0.6	9	3.2	7	2.6

Notes:

[a] Rudnick and Gao, 2014

[b] Jacob et al., 2015; Farmer et al., 2005

[c] Best et al., 2009

[d] Barnes et al., 2001

[e] Christiansen et al., 2007

This is a preprint, the final version is subject to change, of the American Mineralogist (MSA)
Cite as Authors (Year) Title. American Mineralogist, in press.
DOI: https://doi.org/10.2138/am-2018-6256

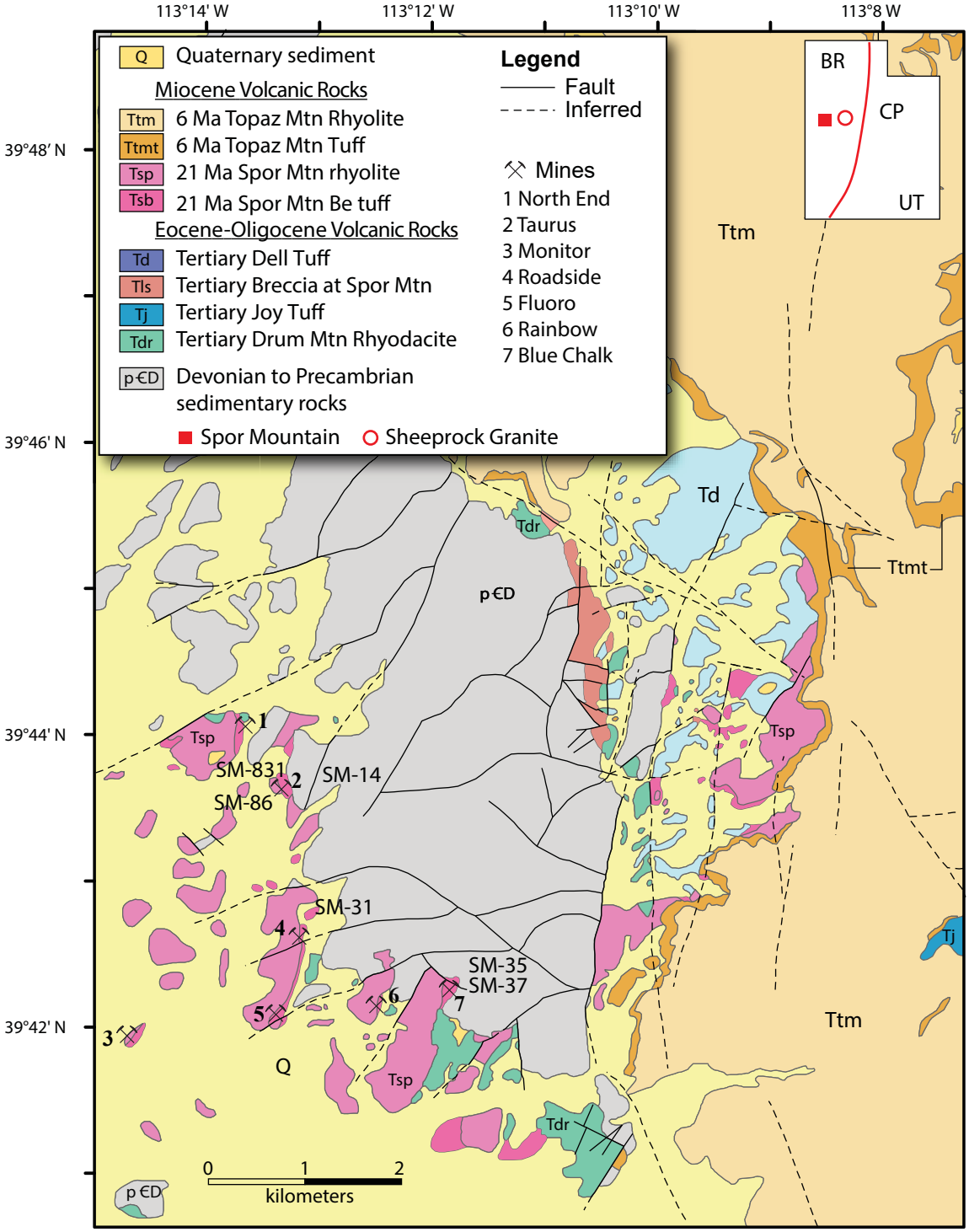

Figure 1

This is a preprint, the final version is subject to change, of the American Mineralogist (MSA)
Cite as Authors (Year) Title. American Mineralogist, in press.
DOI: https://doi.org/10.2138/am-2018-6256

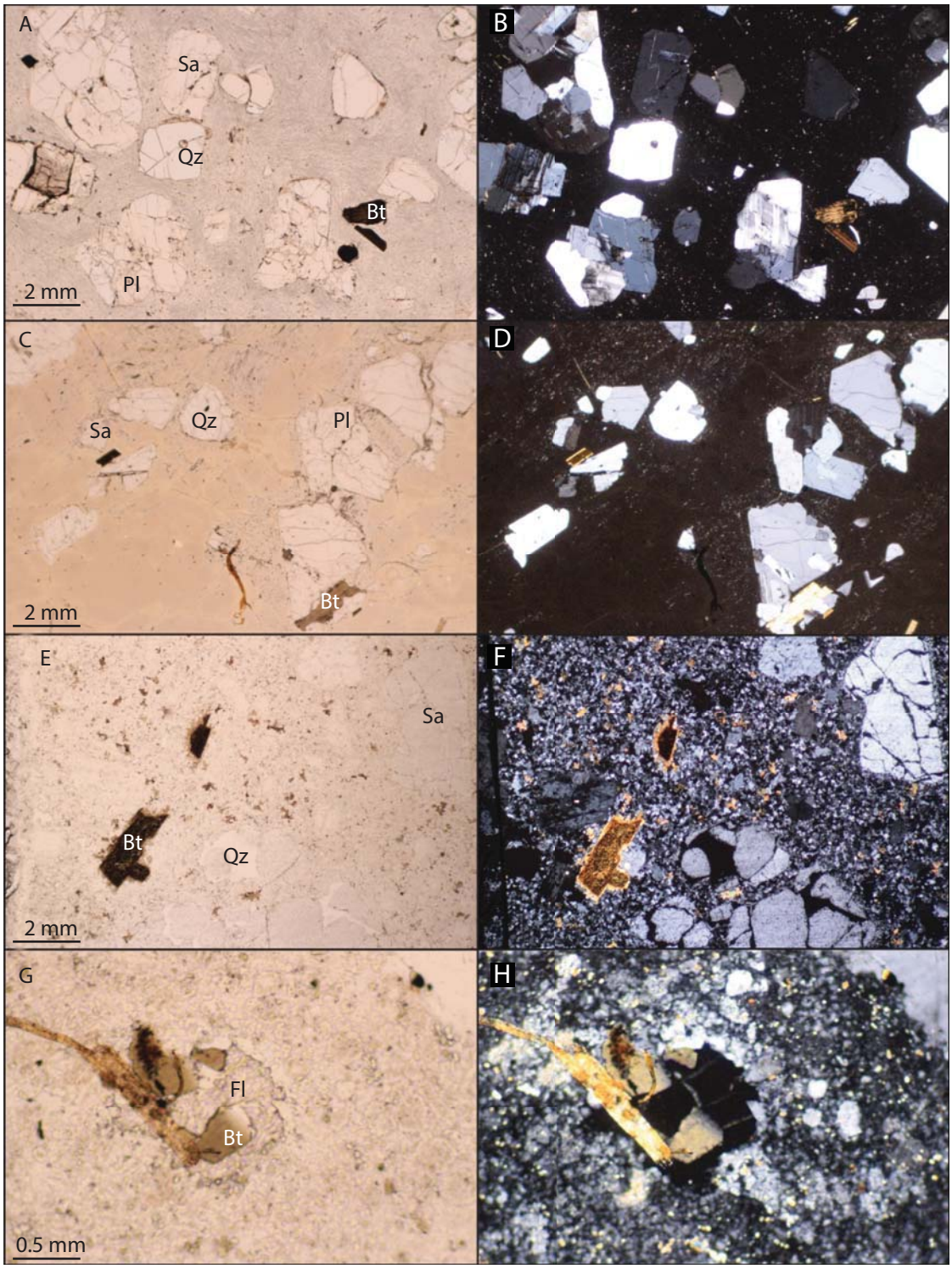

Figure 2

This is a preprint, the final version is subject to change, of the American Mineralogist (MSA)
Cite as Authors (Year) Title. American Mineralogist, in press.
DOI: https://doi.org/10.2138/am-2018-6256

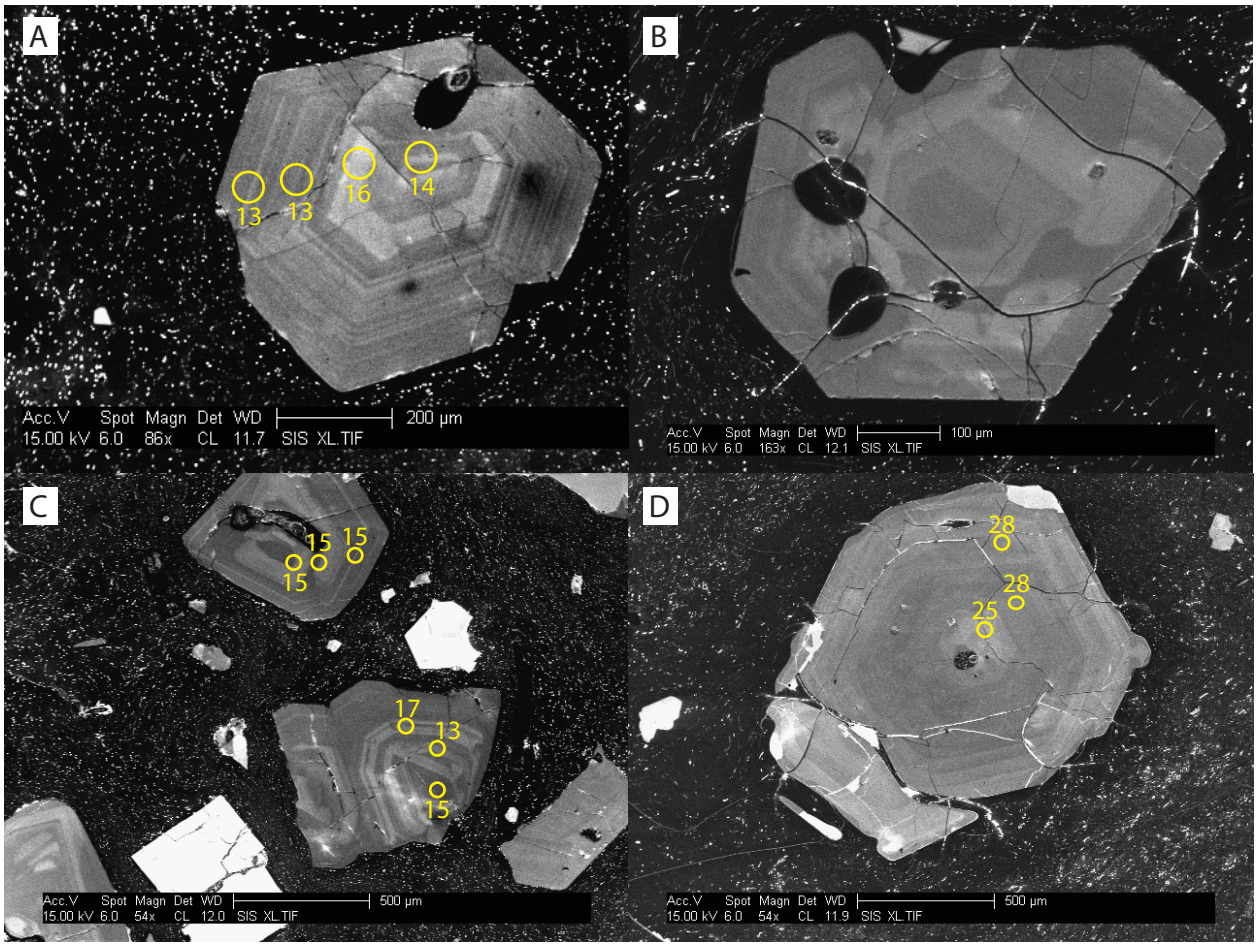

Figure 3

This is a preprint, the final version is subject to change, of the American Mineralogist (MSA)
Cite as Authors (Year) Title. American Mineralogist, in press.
DOI: https://doi.org/10.2138/am-2018-6256

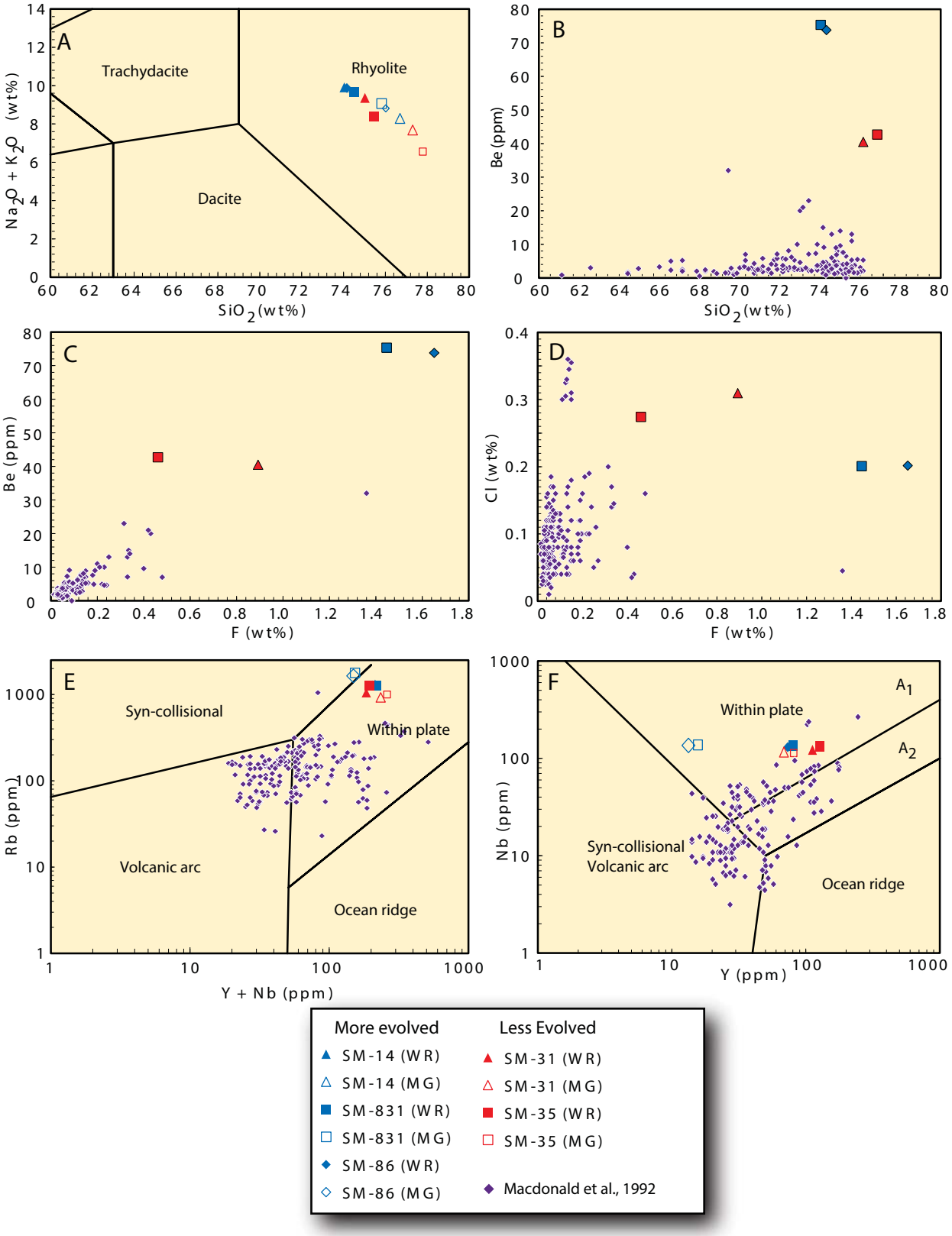

Figure 4

This is a preprint, the final version is subject to change, of the American Mineralogist (MSA)
Cite as Authors (Year) Title. American Mineralogist, in press.
DOI: https://doi.org/10.2138/am-2018-6256

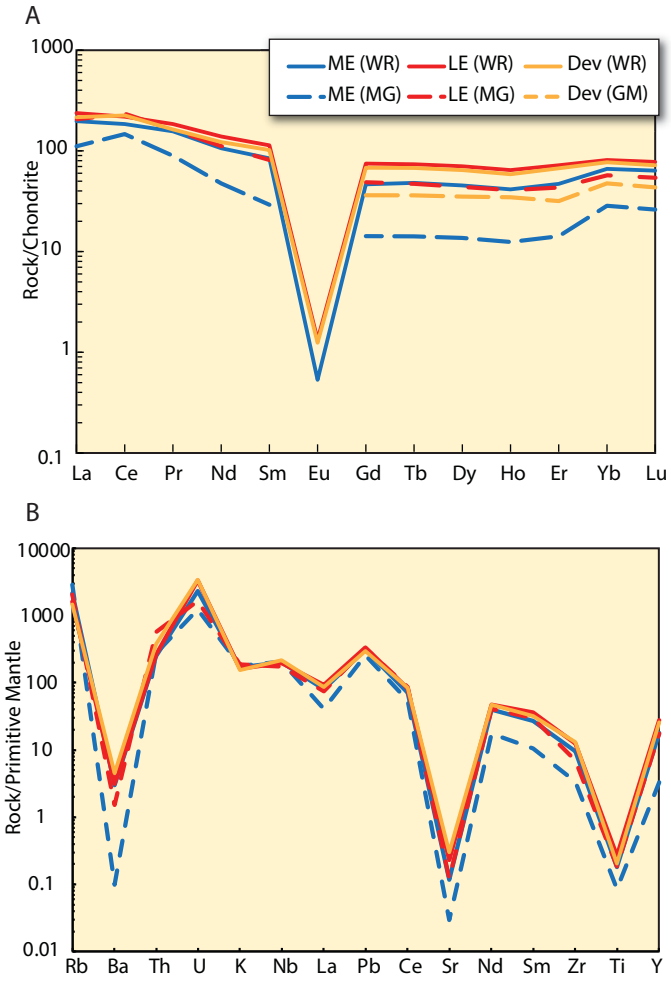

Figure 5

This is a preprint, the final version is subject to change, of the American Mineralogist (MSA)
Cite as Authors (Year) Title. American Mineralogist, in press.
DOI: https://doi.org/10.2138/am-2018-6256

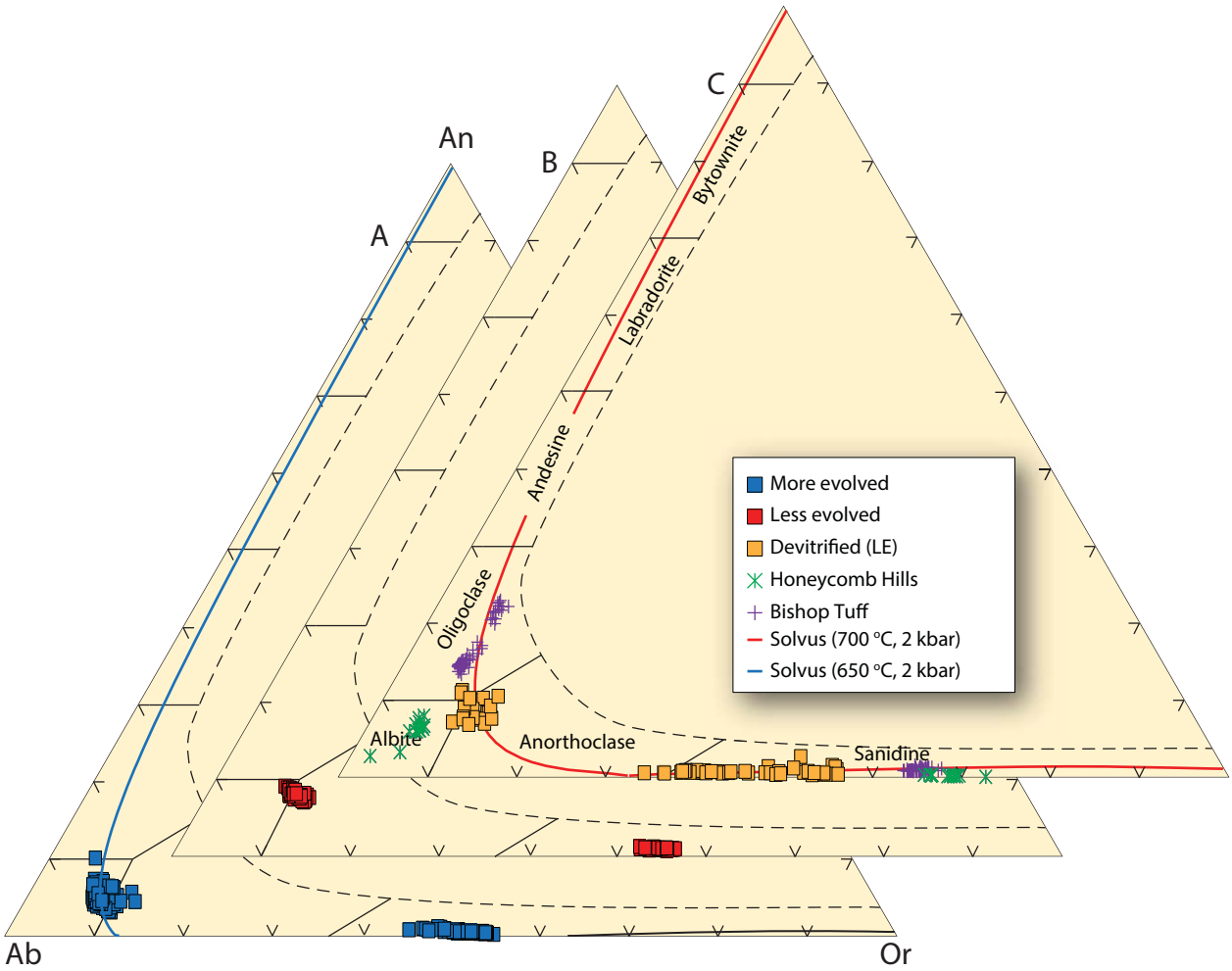

Figure 6

This is a preprint, the final version is subject to change, of the American Mineralogist (MSA)
Cite as Authors (Year) Title. American Mineralogist, in press.
DOI: https://doi.org/10.2138/am-2018-6256

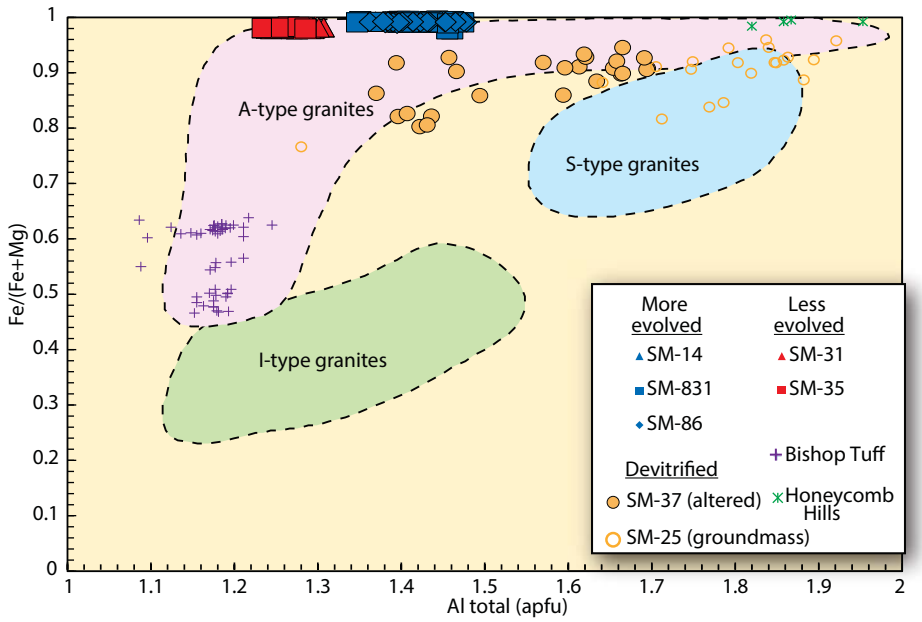

Figure 7

This is a preprint, the final version is subject to change, of the American Mineralogist (MSA)
Cite as Authors (Year) Title. American Mineralogist, in press.
DOI: https://doi.org/10.2138/am-2018-6256

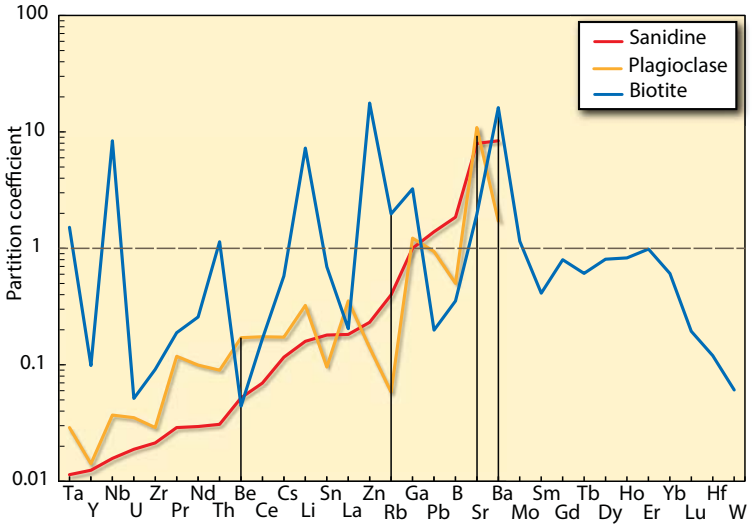

Figure 8

This is a preprint, the final version is subject to change, of the American Mineralogist (MSA)
Cite as Authors (Year) Title. American Mineralogist, in press.
DOI: https://doi.org/10.2138/am-2018-6256

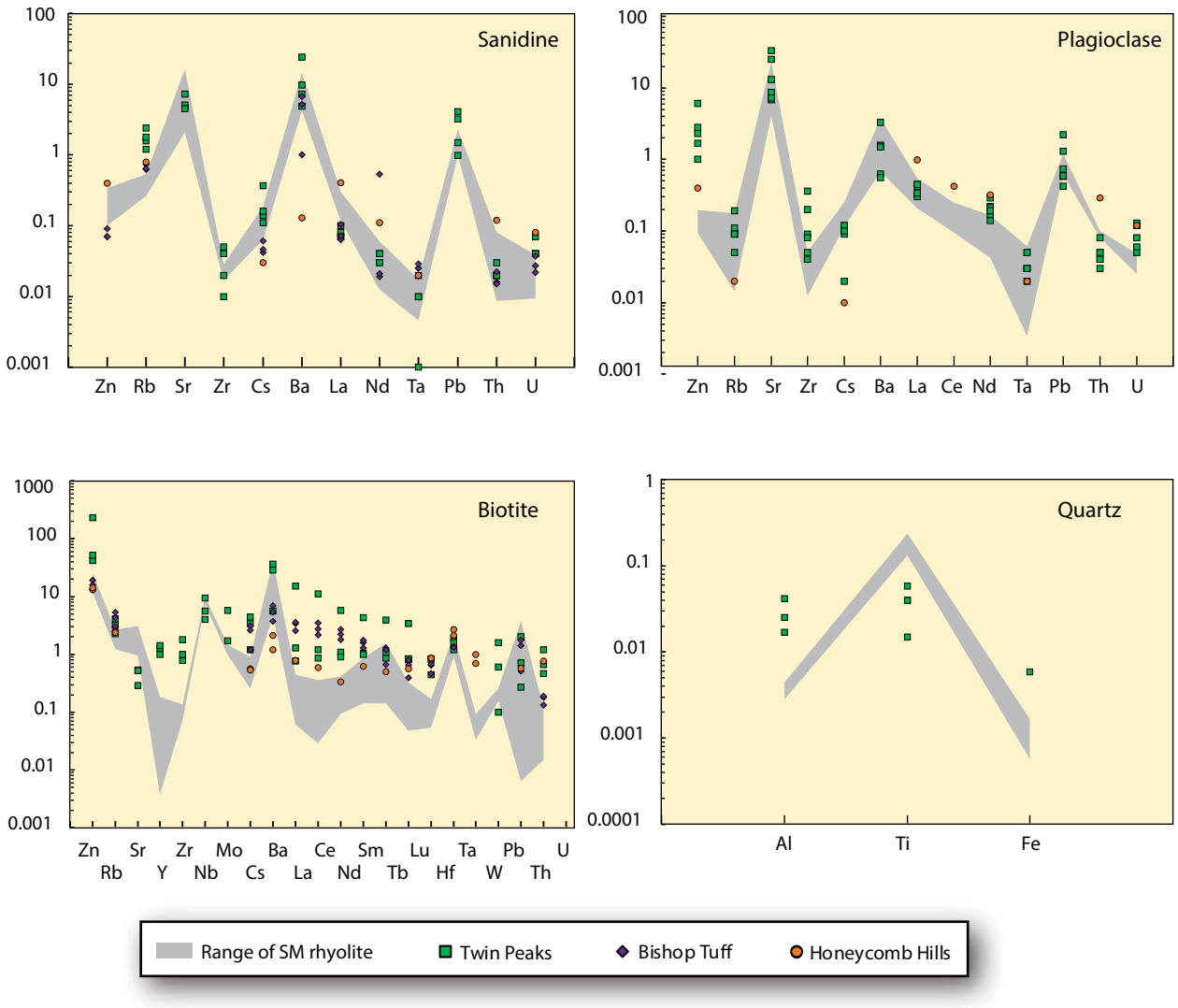

Figure 9

This is a preprint, the final version is subject to change, of the American Mineralogist (MSA)
Cite as Authors (Year) Title. American Mineralogist, in press.
DOI: https://doi.org/10.2138/am-2018-6256

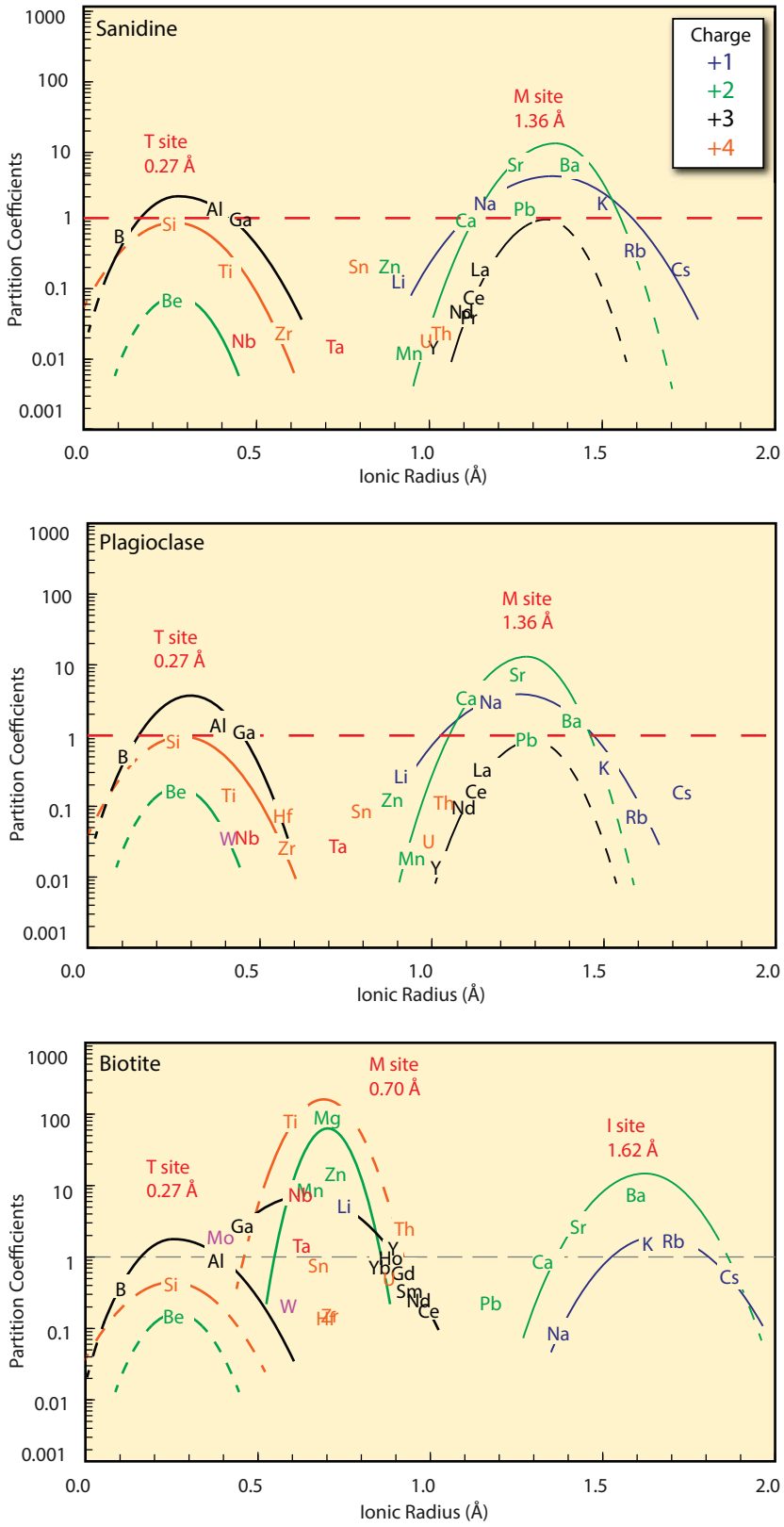

Figure 10

This is a preprint, the final version is subject to change, of the American Mineralogist (MSA)
Cite as Authors (Year) Title. American Mineralogist, in press.
DOI: https://doi.org/10.2138/am-2018-6256

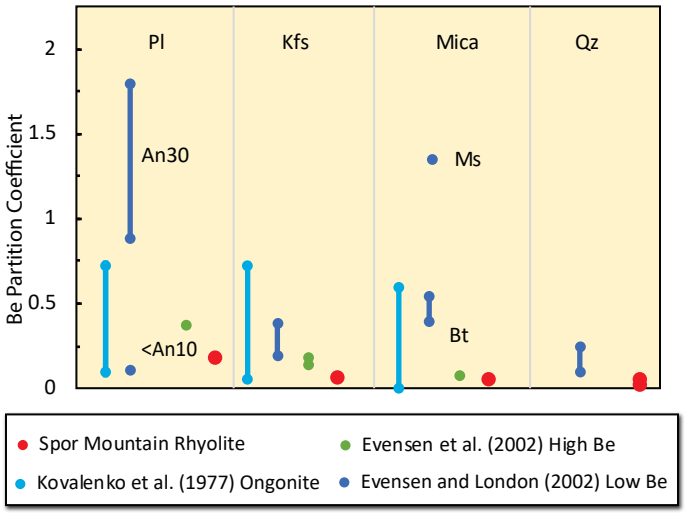

Figure 11

This is a preprint, the final version is subject to change, of the American Mineralogist (MSA)
Cite as Authors (Year) Title. American Mineralogist, in press.
DOI: https://doi.org/10.2138/am-2018-6256

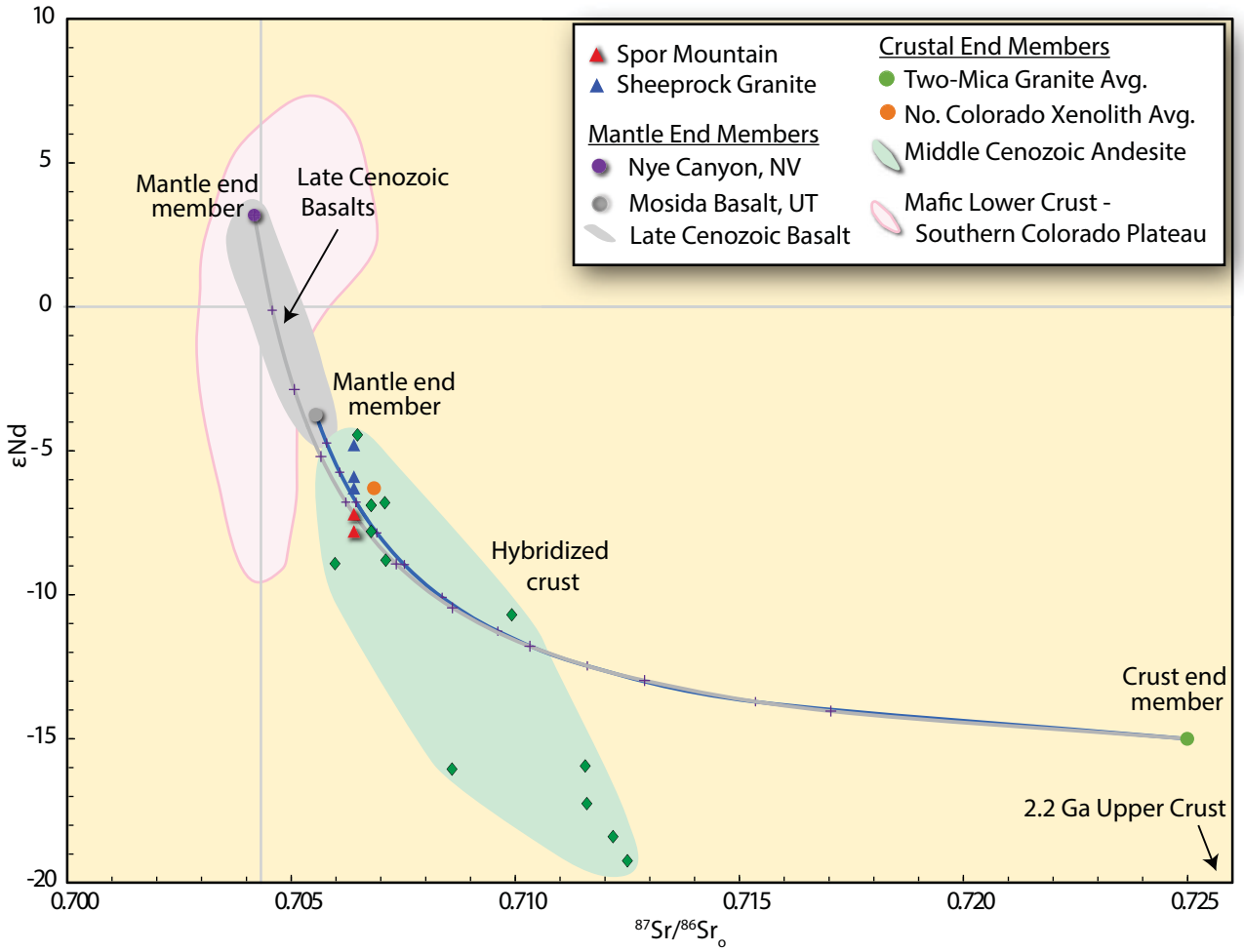

Figure 12

This is a preprint, the final version is subject to change, of the American Mineralogist (MSA)
Cite as Authors (Year) Title. American Mineralogist, in press.
DOI: https://doi.org/10.2138/am-2018-6256

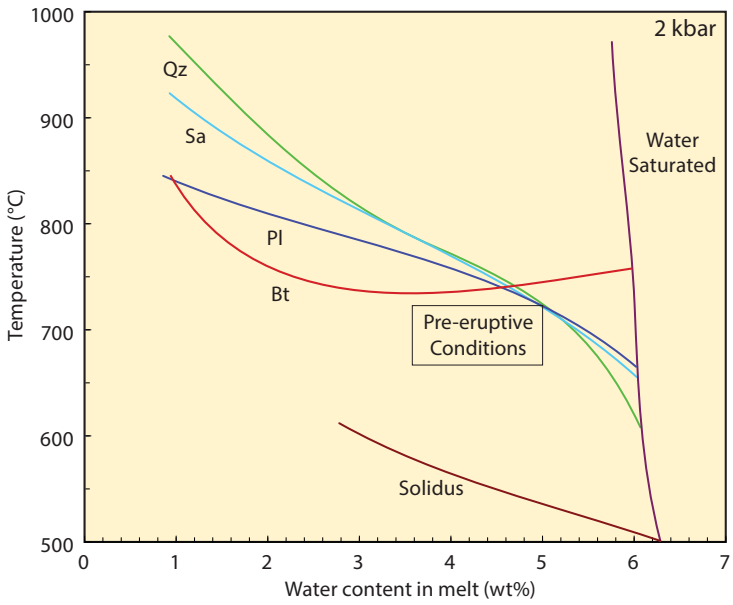

Figure 13

This is a preprint, the final version is subject to change, of the American Mineralogist (MSA)
Cite as Authors (Year) Title. American Mineralogist, in press.
DOI: https://doi.org/10.2138/am-2018-6256

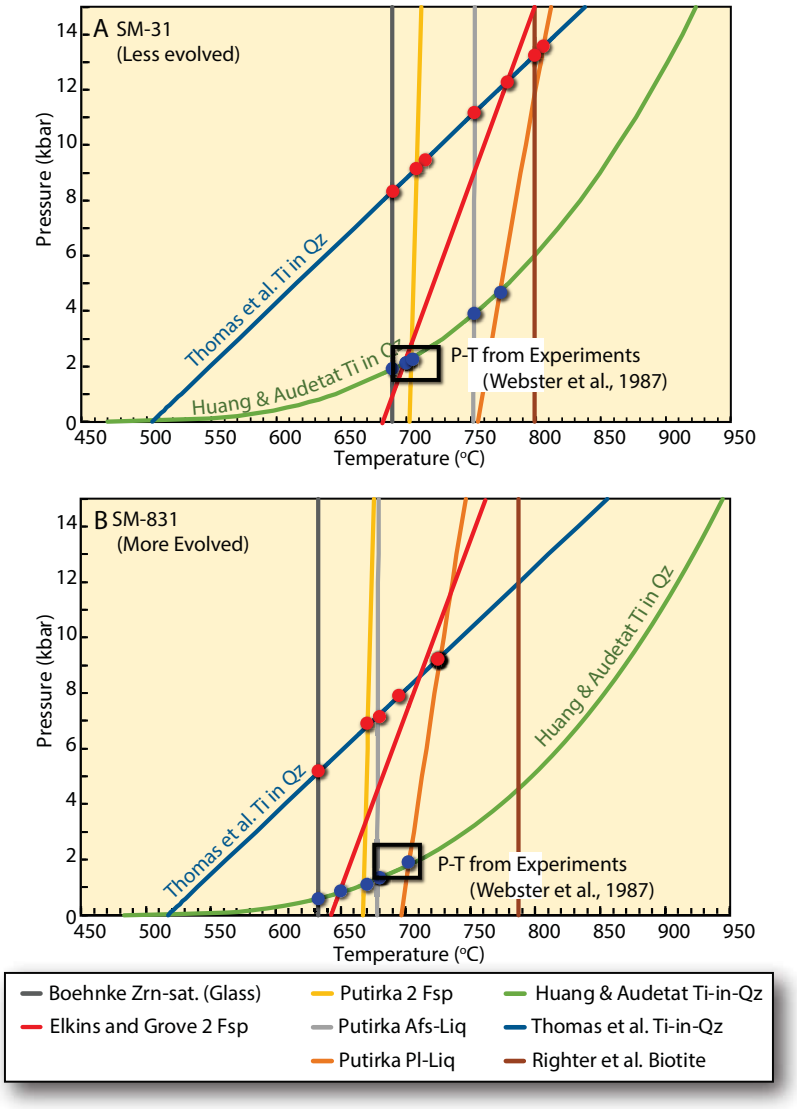

Figure 14

This is a preprint, the final version is subject to change, of the American Mineralogist (MSA)
Cite as Authors (Year) Title. American Mineralogist, in press.
DOI: https://doi.org/10.2138/am-2018-6256

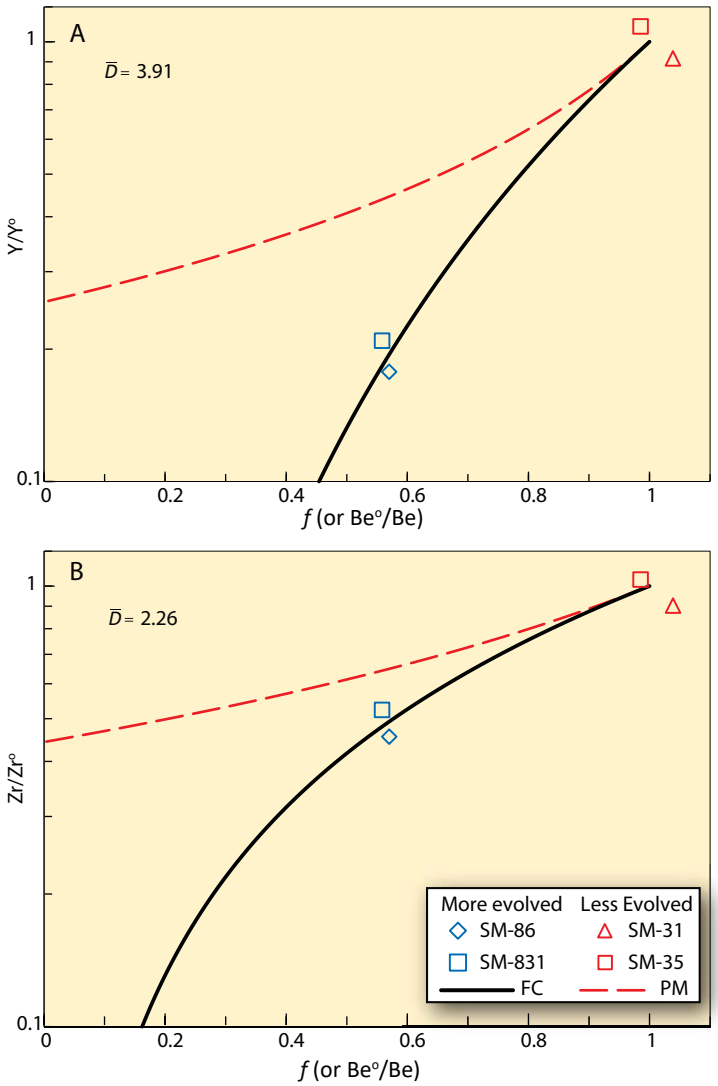

Figure 15

This is a preprint, the final version is subject to change, of the American Mineralogist (MSA)
Cite as Authors (Year) Title. American Mineralogist, in press.
DOI: https://doi.org/10.2138/am-2018-6256

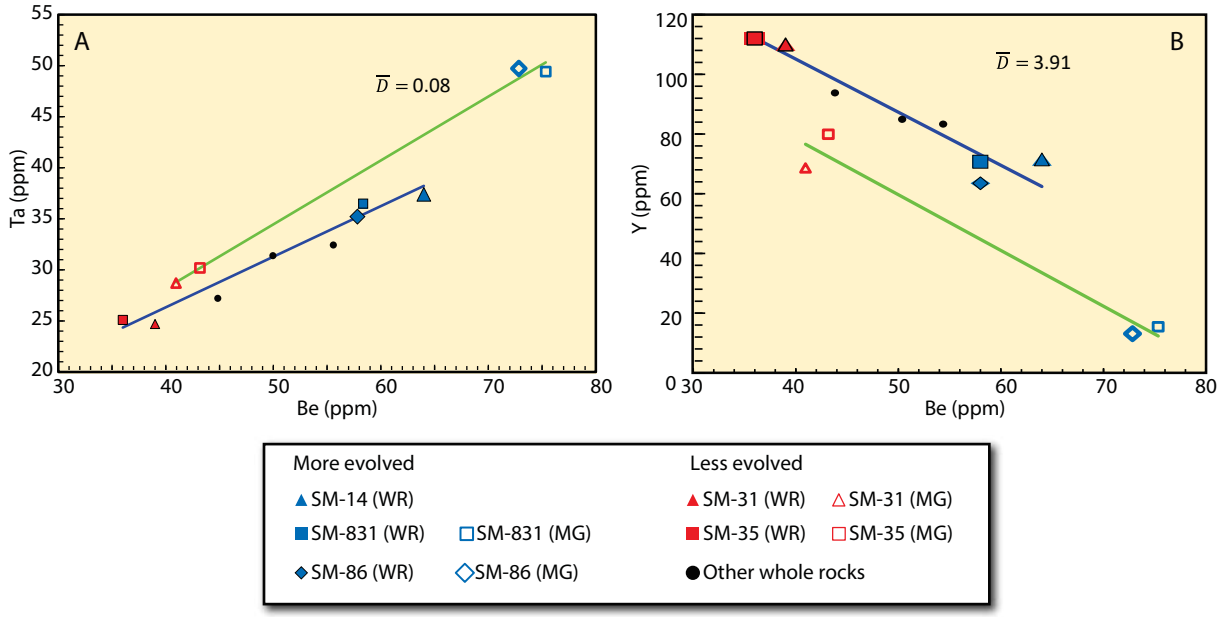

Fig. 16

This is a preprint, the final version is subject to change, of the American Mineralogist (MSA)
Cite as Authors (Year) Title. American Mineralogist, in press.
DOI: https://doi.org/10.2138/am-2018-6256

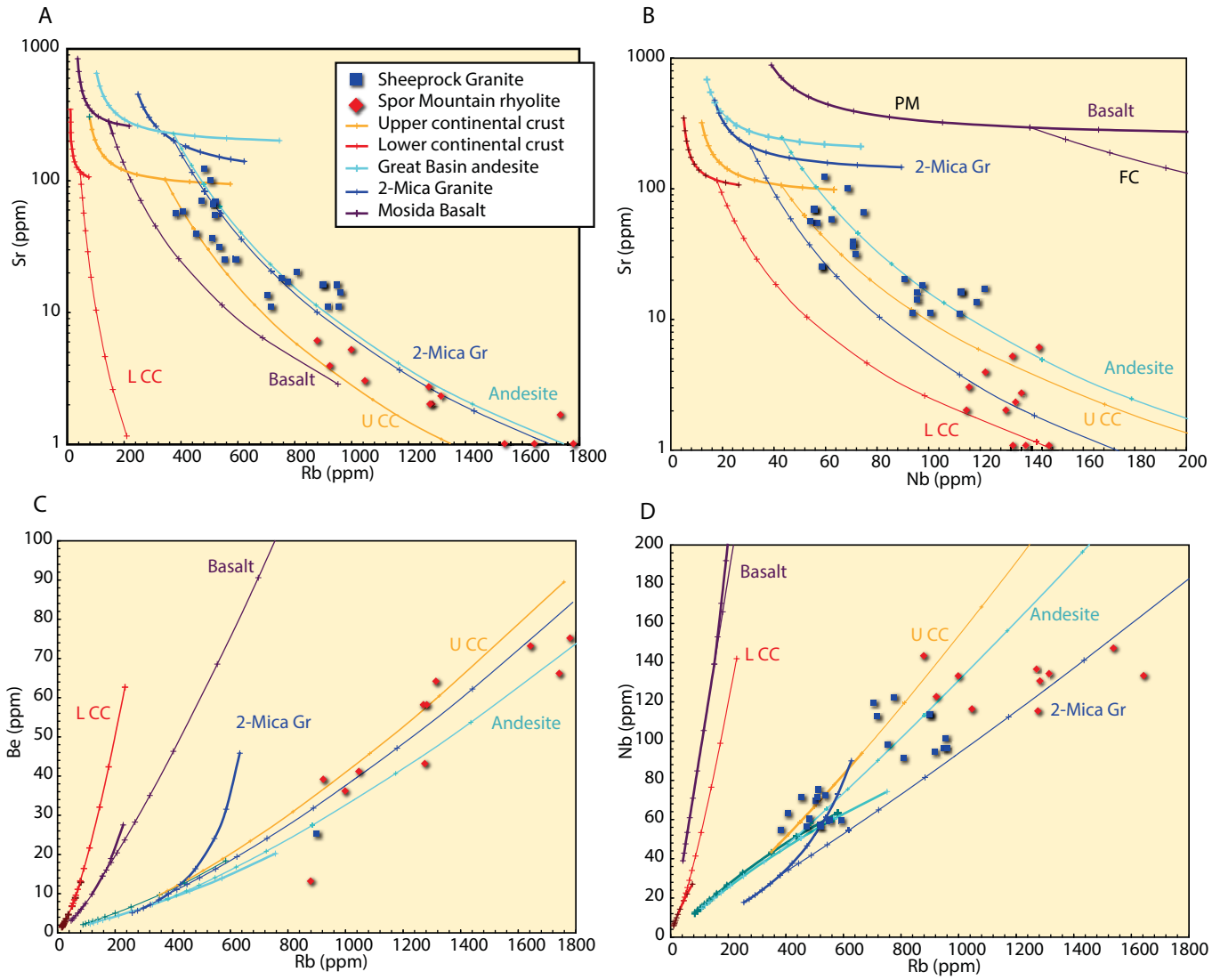

Figure 17